# Contribution of ground ice melting to the expansion of Selin Co (lake) on the Tibetan Plateau

Lingxiao Wang[1], Lin Zhao[1,2], Huayun Zhou[2,3], Shibo Liu[2,3], Erji Du[2], Defu Zou[2], Guangyue Liu[2], Yao Xiao[2], Guojie Hu[2], Chong Wang[1], Zhe Sun[2], Zhibin Li[1], Yongping Qiao[2], Tonghua Wu[2], Chengye Li[1], Xubing Li[1]

[1]School of Geographical Sciences, Nanjing University of Information Science & Technology (NUIST), Nanjing 210044, China
[2]Cryosphere Research Station on Qinghai-Xizang Plateau, State Key Laboratory of Cryosphere Science, Northwest Institute of Eco-Environment and Resources, Chinese Academy of Sciences (CAS), Lanzhou, 730000, China
[3]University of Chinese Academy of Sciences, Beijing, China

*Correspondence to*: Lin Zhao (lzhao@nuist.edu.cn)

**Abstract.** Selin Co, located within permafrost regions surrounded by glaciers, has exhibited the greatest increase in water storage among all the lakes on the Tibetan Plateau over the last 50 years. Most of the increased lake water volume has been attributed to increased precipitation and the accelerated melting of glacier ice, but these processes are still not sufficient to achieve the water balance with the expansion of Selin Co. Ground ice meltwater released by thawing permafrost due to continuous climate warming over the past several decades was regarded as another source of lake expansion. This study presented the first attempt to quantify the water contribution of ground ice melting to the expansion of Selin Co by evaluating the ground surface deformation. We monitored the spatial distribution of surface deformation in the Selin Co basin using the SBAS-InSAR technique and compared the results with the findings of field surveys. Then, the ground ice meltwater volume in the watershed was calculated based on the cumulated settlement. Finally, this volume was compared with the lake volume change during the same period, and the contribution ratio was derived. SBAS-InSAR monitoring during 2017–2020 illustrated widespread and large subsidence in the upstream section of the Zhajiazangbu subbasin, where widespread continuous permafrost is present. The terrain subsidence rate was normally between 5 and 20 mm/a, indicating rapid ground ice loss in the region. The ground ice melted water reached a rate of $57.4 \times 10^6$ m$^3$/a, and the rate of increase in lake water storage was $485 \times 10^6$ m$^3$/a during the same period, with ground ice meltwater contributing 11.8% of the lake volume increase. This study is especially helpful for explaining the rapid expansion of Selin Co and equilibrating the water balance at the watershed scale. More importantly, the proposed method can be easily extended to other watersheds underlain by permafrost and to help understand the hydrological changes in these watersheds.

**Keywords:** surface deformation, SBAS-InSAR, permafrost, ground ice, Selin Co, expansion

## 1. Introduction

35   More than 1200 lakes on the Tibetan Plateau (TP) span an area exceeding 1 km$^2$, and the total lake area is greater than 46000 km$^2$ (Zhang et al., 2021b). The water in most of these lakes is more or less connected with widely distributed glaciers and permafrost. Recent studies have indicated that most of the lakes on the TP have manifested extensive changes (Qiao et al., 2019; Zhang et al., 2020). In particular, Selin Co (also known as Siling Co, Serlin Co, and Serling Co) exhibited the greatest increases in both lake area and water storage:

40   its lake area expanded by ~40% from ~1700 km$^2$ in 1972 to ~2400 km$^2$ in 2020, and its water storage increased by 80% from 309.4×10$^8$ m$^3$ in 1972 to 558.4×10$^8$ m$^3$ in 2017 (Zhu et al., 2019b; Zhang et al., 2021b). Its lake area surpassed that of Nam Co in the early 2000s (Zhang et al., 2021b; Bian et al., 2010); consequently, Selin Co is now the second largest saltwater lake in China. Such rapid changes in Selin Co have significantly affected the regional environment and have thus attracted substantial interest within the

45   scientific community.

The entire Selin Co watershed covers a drainage area of 4.4×10$^4$ km$^2$, 18 times the lake surface. Accordingly, a lake water level increase of 0.2 m/a corresponds to at least 1 cm/a of water collected uniformly over the whole watershed area (neglecting evaporation). The entire watershed hosts 299 glaciers with a total area of

50   369.7 km$^2$ and ice reserves of 27.9 km$^3$ based on the second Chinese glacier inventory (Guo et al., 2015; Liu et al., 2012b); additionally, according to the new estimation by (Farinotti et al., 2019), the glacier volume reaches 21.8 km$^3$ in the watershed. (Zou et al., 2017) mapped the permafrost distribution on the Qinghai-Tibet Plateau (QTP) based on freezing and thawing indices from Moderate Resolution Imaging Spectroradiometer (MODIS) land surface temperatures and validated their map using various ground-based

55   datasets; according to this permafrost map, the permafrost area covers ~1.3×10$^4$ km$^2$, accounting for 30.2% of the watershed. Continuous permafrost and seasonally frozen ground exist, with the former being widespread mainly in the northern part of the watershed (Zou et al., 2017). (Zhao and Sheng, 2019) estimated the ground ice storage on the QTP based on the ice content distribution characteristics from 164 drill core records deeper than 15 m, the above permafrost distribution map, a map of the Quaternary sedimentary types,

60   and a permafrost thickness map; based on their map, the ground ice volume in the watershed reaches 132.3 km$^3$ (Zhao and Sheng, 2019), approximately five times the glacier ice volume in the Selin Co watershed.

To reveal the potential reasons for the abovementioned rapid expansion of lakes on the TP, an accurate estimation of the basin water balance is urgently needed (Lei et al., 2014; Zhang et al., 2017; Li et al., 2014;

65   Song et al., 2014). Glacial meltwater, the thawing of permafrost, precipitation (including snow) and changes in evapotranspiration all contribute to lake recharge. A model simulation of endorheic basins on the TP showed that increased net precipitation contributed the majority of the water supply (~70%) to the increased lake volume (Zhang et al., 2017). In addition, recent research has revealed that glacial meltwater has contributed ~ 10% of the total water input to Selin Co since the 1970s (Lei et al., 2013; Tong et al., 2016;

70   Brun et al., 2020; Zhang et al., 2021a). The weakening of lake evaporation during 1972–2010 due to

decreasing wind speeds also contributed to the accelerated expansion of Selin Co to some extent, but this contribution was reported to be very small (Guo et al., 2019).

Significant permafrost degradation has been observed on the TP under the impacts of the warming climate. The monitoring of ten boreholes on the TP revealed that from 1981 to 2018, the active layer thickened at an average rate of 19.5 cm per decade; moreover, this thickening trend has been accelerating in recent years (Zhao et al., 2020). In the meantime, different permafrost regions across the TP experienced thaw settlements (Daout et al., 2017; Chen et al., 2022). The ice content within the uppermost layer of permafrost is typically higher than the saturated water content after this permafrost layer thaws; hence, the thawing of this layer might result in terrain settlement (Streletskiy et al., 2016; Shiklomanov et al., 2013; Günther et al., 2015; Lantuit and Pollard, 2008; Kokelj and Jorgenson, 2013). The terrain settlement was attributed to the melting of ground ice from the ice-rich permafrost layer just below the permafrost table and the further release of this water into the hydrological cycle (Zhao et al., 2019).

The melting of ground ice released water into the hydrological cycle (Zhao et al., 2019; Jin et al., 2022), hence permafrost degradation might be a possible source of the water that is causing lakes to expand (Li et al., 2014), but this contribution has yet to be quantified. By separating hydrographs using isotopes, some researchers calculated the contributions of meltwater from ground ice to surface water runoff and found that the contribution ranged from 13.2% to 16.7% in the source region of the Yellow River (Yang et al., 2019), and that to nearby thermokarst lakes in the Beiluhe region reached 61.3% (Yang et al., 2016). The amount of meltwater from permafrost degradation was also modeled by multiplying the active layer thickening rate and the average ground ice content (Zhang et al., 2017).

Interferometric synthetic aperture radar (InSAR) analysis can exploit the phase changes in SAR signals to determine relative surface displacements on the order of millimeters to centimeters. Accordingly, InSAR monitoring can detect the terrain subsidence triggered by the thawing of ice-rich permafrost, e.g., (Daout et al., 2020; Zwieback and Meyer, 2021; Chen et al., 2018; Lu et al., 2020; Liu et al., 2012a). Permafrost regions with higher ground ice contents have been shown to produce greater terrain subsidence on the TP (Wu et al., 2018; Daout et al., 2017; Chen et al., 2018). The subsidence rate is less than 5 mm/a in the northwestern TP, where the climate is cold and dry (Daout et al., 2017), while it is up to 30 mm/a on the ice-rich Eboling Mountain in the northeastern region of the TP (Chen et al., 2018).

In this study, we conducted the first attempt to quantify the contribution of ground ice melting to the expansion of the Selin Co watershed through surface settlement. It is well known that the permafrost layer just below the permafrost table always contains ground ice higher than 50% in volume (Cheng, 1983; Mackay, 1983; French and Harbor, 2013; Zhao and Sheng, 2019). Therefore, we assumed that the amount of surface settlement would release the same amount of ground ice caused by compressing the thawing ice-rich

permafrost layer. The spatial distribution of surface deformation was derived through InSAR analysis and compared with the findings of field surveys. Finally, the ground ice meltwater volume in the watershed was compared with the Selin Co volume increase, and the contribution ratio was determined.

## 2. Study area and data resources

### 2.1 Study area

The Selin Co watershed, which is in the transitional zone between the Indian monsoon and the westerlies over the TP, is characterized by a cold semiarid monsoon climate with a mean annual temperature of approximately 0°C and average precipitation of ~350 mm (Tong et al., 2016). From 1979 to 2017, the average annual temperature increased at a rate of 0.049°C/a, and the average annual precipitation increased at a rate of 4.65 mm/a, with the main increase occurring after the mid-1990s (Zhu et al., 2019b).

This watershed basin extends over a total area of approximately $4.4 \times 10^4$ km$^2$, and the rivers and lakes within the basin are connected, forming an inland lake group. Ngoin Co is located south of Selin Co, while Wuru Co & Qiagui Co are located west of Selin Co; their locations are marked as ② and ③, respectively, in Fig. 1. The main rivers draining into the lake are the Zhajiazangbu (from the north), the Zhagenzangbu and Alizangbu (from the west), and the Boquzangbu (from the east) (Tong et al., 2016), as shown in Fig. 1. The details of the four major subbasins and the inflows of the runoff from these rivers into the lake are listed in Table 1. The Zhajiazangbu river with a length of 409 km originates from the Tanggula Mountains and enters Selin Co from the north. Widespread continuous permafrost occurs mainly in the northern part of the basin, whereas sporadic permafrost and seasonally frozen ground are found in the central and southern parts of the watershed. Among the four subbasins, the Zhajiazangbu has the largest permafrost distribution (10667 km$^2$ or 66.2% of the subbasin area), followed by the Zhagenzangbu (1967 km$^2$ or 12.3% of the subbasin area) (Zou et al., 2017).
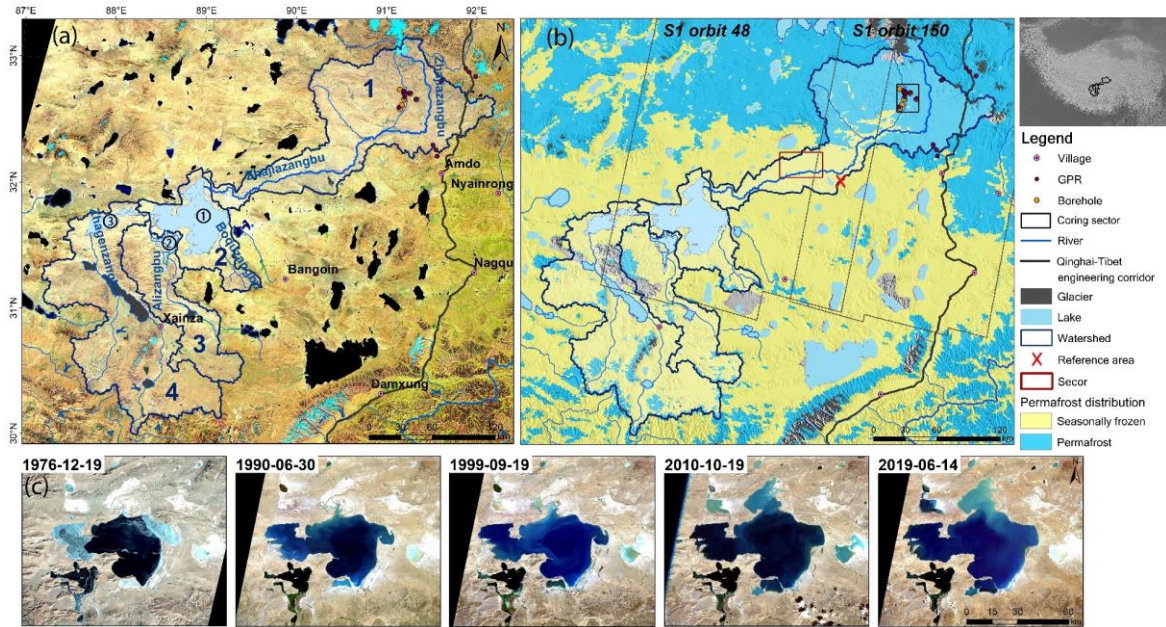
**Figure 1 Study area. The base map in Fig. 1(a) is a Landsat 8 image acquired in October 2020 (red: SWIR1, green: NIR, blue: red). The base map in Fig. 1(b) is a permafrost map (Zou et al., 2017); the hillshade is calculated using a 1-arcsec SRTM DEM with the Sentinel-1 incidence angle and azimuth angle. The grey dashed lines delineate two tracks of Sentinel-1 used in this study. The red cross marks the position of our InSAR reference point. The locations of the GPR surveys and boreholes are shown with dots. Fig. 1(c) shows the lake areas from 1976 to 2019 on Landsat optical images.**

135

**Table 1 Characteristics of the Selin Co basin.**

| Basin | | Area (km$^2$) | Average elevation (m a.s.l.) | Permafrost coverage | | |
|---|---|---|---|---|---|---|
| | | | | Area (km$^2$) | Percentage of subbasin area (%) | Percentage of the entire basin area (%) |
| **1** | Zhajiazangbu subbasin | 16112 | 4963 | 10667 | 66.2 | 24 |
| **2** | Boquzangbu subbasin | 5474 | 4651 | 124 | 2.3 | 0.3 |
| **3** | Alizangbu subbasin | 6831 | 4951 | 646 | 9.5 | 1.5 |
| **4** | Zhagenzangbu subbasin | 16019 | 5022 | 1967 | 12.3 | 4.4 |
| | Entire basin | 44437 | 4944 | 13404 | | 30.2 |

140

## 2.2 Field data

We conducted a field investigation of the permafrost in the study area in October 2019. Seven boreholes deeper than 20 m were drilled, and ground-penetrating radar (GPR) surveys were carried out in the upstream

section of the Zhajiazangbu subbasin (locations are marked in Fig. 1). The survey was performed at the end

145   of the thawing period, allowing us to estimate the maximum thawing depth and the location of the permafrost table. The permafrost table was estimated from the cores of the boreholes, and the development of ground ice was described as well. Descriptions of the boreholes are provided in Table 2, and field photographs of the cores at borehole sites SLC01 and SLC04 are shown in Fig. 2.

150   Twenty 50-m-long GPR profiles were carried out within or around the catchment, fourteen of which were within the basin. Based on the fourteen GPR profiles carried out within the basin, the permafrost table was at a maximum depth of 4.1 m, a minimum depth of 2.0 m, and an average depth of 3.2 m. The volumetric soil water content in the active layer ranged from a maximum of 46.4% to a minimum of 14.7%, with an average of 22.6% based on our interpretation of the GPR data.

155
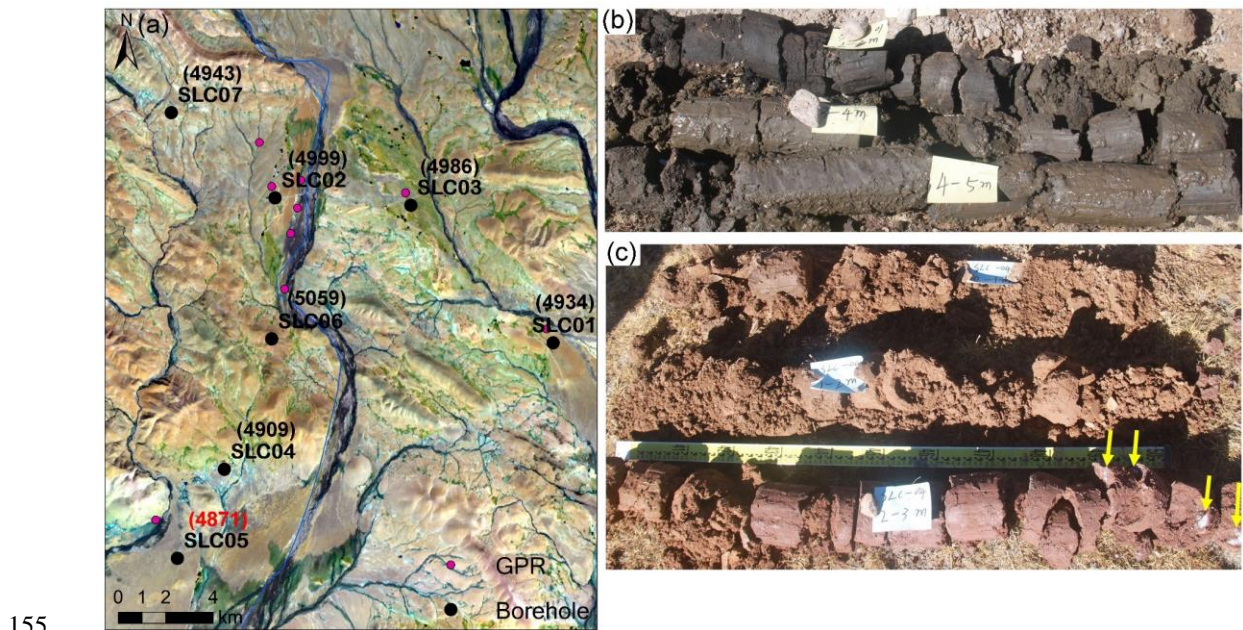
**Figure 2 (a) Locations of surveyed sites. The base map is Landsat 8 image acquired in October 2020. For borehole sites, their elevations (m a.s.l.) are labeled in brackets. Site SLC05 has no permafrost. Cores from borehole SLC01 at depths of 2–5 m (a) and SLC04 at depths of 0–3 m (b). Ice blocks were found in SLC04 at a depth of 2.4 m, as indicated by the arrows in (b).**

160

**Table 2 Borehole properties.**

| Site | Permafrost table depth (m) | Topography | Surface | Development of ground ice |
|------|------|------|------|------|
| **SLC01** | 3.0 | floodplain | alpine meadow veg coverage: 40%, surface soil is sandy, dry | Not found |
| **SLC02** | 3.6 | river terrace | degraded alpine steppe, | ice at depths of 3.6–5.5 m |

| | | | sparse vegetation, surface soil is sandy, dry | |
|---|---|---|---|---|
| SLC03 | 3.0 | river valley | alpine swamp meadow, veg coverage: 90% high water content in the active layer | ice at 2.4–3.0 m, large amounts of liquid water found at 3.0–4.5 m, ice lenses at 4.6–5.1 m |
| SLC04 | < 2.4 | river valley terrace, approximately 500 m away from the river | alpine swamp meadows veg coverage: 90% | ice at 2.4 m, pure ice layer (~3 cm) at 4.2–4.3 m, ice lenses at 6–7.7 m |
| SLC05 | N/A seasonally frozen ground | river valley in between two rivers | alpine steppe veg coverage: 30%, surface soil is sandy and contains abundant gravel | not found |
| SLC06 | unclear | top of slope | alpine meadow veg coverage: 50%, surface soil is sandy and contains abundant gravel | ice at 6–7.8 m |
| SLC07 | unclear | middle of a very gentle slope | degraded alpine meadow, very sparse veg surface soil is sandy and contains abundant gravel, severely salinized | liquid water found at 2.5–6.5 m, a large amount found at 2.5–3.5 m |

## 2.3 Sentinel-1 SAR images

Sentinel-1 (S1) C-band SAR images (https://scihub.copernicus.eu/) were used to monitor the surface
deformation. S1, a constellation comprising two satellites launched in 2014 (S1A) and 2016 (S1B) that orbit
the Earth, is a C-band SAR mission that was developed and is operated by the European Space Agency (ESA)
as part of the Copernicus program. VV-polarized Level 1 single look complex (SLC) images acquired in
interferometric wide-swath (IW) mode in descending orbit were used in the study. The study area is covered
by two orbits of S1 acquisitions, the details of which are shown in Table 3. In total, 95 acquisition dates for
descending orbit 48 and 100 acquisition dates for descending orbit 150 from September 2017 to December
2020 were processed.

**Table 3 Information on the S1 images processed to monitor the surface deformation.**

| | Orbit 48 | Orbit 150 |
|---|---|---|
| **Frame** | 489, 484, 479 | 490, 485, 480 |
| **Incidence angle range (degrees)** | 31.85–46.32 | 31.57–46.27 |
| **Acquisition period** | 20170911 to 20201224 | 20170905 to 20201230 |

| Number of acquisition dates | 95 | 100 |
|---|---|---|

## 2.4 SRTM DEM

A 1-arcsecond grid (~30-m) Shuttle Radar Topographic Mission (SRTM) digital elevation model (DEM) was used to calculate the slope, and remove the topographic phase and implement geocoding during InSAR processing.

## 2.5 ICESat-2 dataset

Laser altimetry data from the ICESat-2 ATL13 product (https://nsidc.org/data/atl13) were applied to extract the water surface elevations of the lakes.

## 2.6 Landsat 8 Operational Land Imager (OLI) images

Optical Landsat 8 OLI images (https://glovis.usgs.gov/) were used to detect changes in the lake extents. Cloud-free images acquired during autumn or summer were selected, and the acquisition date and path/row of each image are listed in Table 4.

**Table 4 Information on the Landsat 8 images used.**

| Lake | 2015 | 2016 | 2017 | 2018 | 2019 | 2020 |
|---|---|---|---|---|---|---|
| **Selin Co** | p140r037 D20151117 | p139r038 D20161112 | p139r038 D20170928 | p139r038 D20181001 | p139r038 D20190614 | p139r038 D20201006 |
| **Ngoin Co** | p140r038 D20150930 | p139r038 D20161112 | p139r038 D20170928 | p140r038 D20181109 | p140r038 D20190925 | p140r038 D20201013 |
| **Wuru Co & Qiagui Co** | p140r038 D20150930 | p140r038 D20161103 | p140r038 D20171005 | p140r038 D20181109 | p140r038 D20190925 | p140r038 D20201013 |

"p" denotes the path, "r" denotes the row of the frame, and "D" denotes the acquisition date.

## 3 Methodology

### 3.1 Workflow

An overview of the methodology employed in this study is illustrated in Fig. 3. The main steps are summarized as i) retrieval of lake water storage changes, ii) retrieval of deformation time series, iii) estimation of the ground ice meltwater volume from the long-term deformation rate, and iv) calculation of the ratio of the water volume contributed by permafrost ground ice melting to the increase in lake water storage. The processing steps are described in detail in the following subsections.
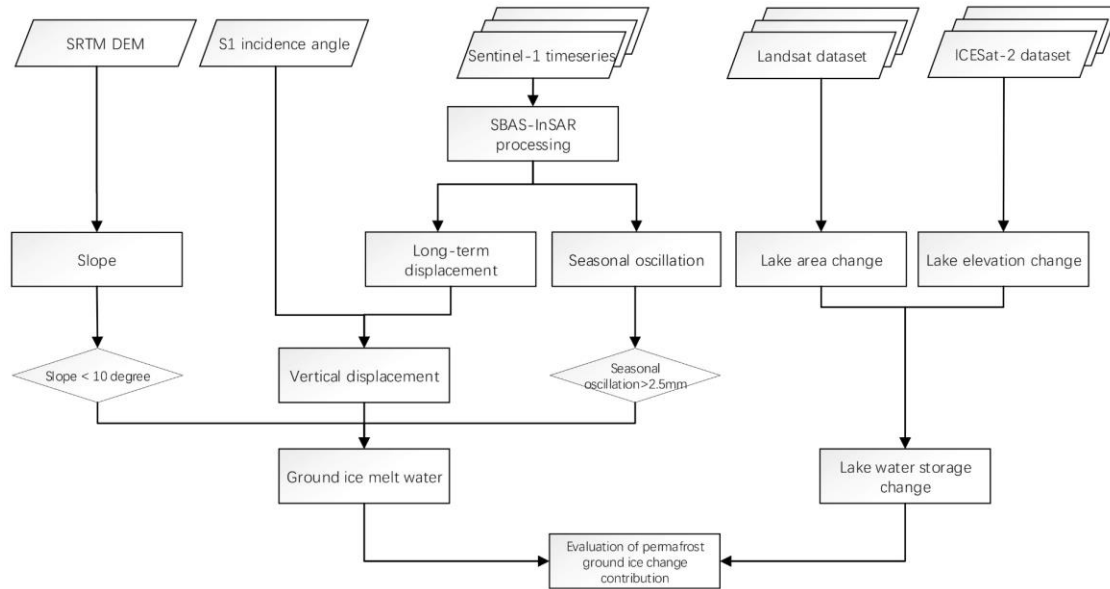
**Figure 3 Workflow of estimating the water contribution by permafrost ground ice melting to the expansion of Selin Co.**

200

## 3.2 Lake water storage changes

First, we retrieved water surface elevations through the ICESat-2 ATL13 laser altimetry product by extracting data values within each lake's area from 13 October 2018 to the end of 2020. For each year, the mean annual elevation was calculated from all data acquisitions during the year. The lake water level change rate was then

205    estimated by a linear trend model.

Then, we extracted the lake area extent using Landsat 8 OLI images in 2018, 2019, and 2020. Three bands (NIR, SWIR1, and SWIR2) were stacked to extract the lake area because lake water has extremely low reflectance in these bands and thus is easily separated from other land cover types. K-means clustering was

210    then applied to classify the land cover types in the stacked image into two classes: water and other. After that, a 3×3 window size majority filtering was applied as a postprocessing step, and we then converted the classified image into a shapefile and eliminated the spots outside the inlet and outlets of the lakes. The lake areas in 2015, 2016 and 2017 were obtained from a previous study (Zhang, 2019); we also modified the lakes to have the same inlets and outlets. For lakes with irregular areas, their storage was approximately calculated

215    according to the volume of a circular platform; thus, the change in the volume of the lake was calculated from the difference between the volumes of two circular platforms (Zhang et al., 2019a), as described in Eq. (1):

$$\Delta V = \frac{1}{3}(H_2 - H_1) \times \left(S_1 + S_2 + \sqrt{S_1 \times S_2}\right) \tag{1}$$

where $\Delta V$ is the change in lake water storage, $S_1$ and $S_2$ represent the lake areas during two periods (e.g., the lake areas in 2018 and 2020), and $(H_2 - H_1)$ represents the water surface elevation change between the two periods.

### 3.3 Deformation monitoring

### 3.3.1 SBAS-InSAR processing

In this study, we implemented the small baseline subset (SBAS) time series InSAR analysis (SBAS-InSAR) technique, which deploys multiple master datasets to minimize the effects of spatiotemporal decorrelation (Berardino et al., 2002; Lanari et al., 2004; Usai, 2003) by selecting interferograms with small spatial and temporal baselines. Thus, this technique is suitable for permafrost environments prone to strong spatiotemporal decorrelation.

The Selin Co basin is covered by two orbits of S1 images. We processed the SBAS-InSAR analysis individually for each orbit. SBAS-InSAR processing in this study contains three main steps: i) InSAR processing of the images, including interferogram network selection, coregistration, differential interferogram phase generation and phase unwrapping; ii) deformation time series estimation; and iii) reference point refinement and geocoding.

The main processing steps are described in detail as follows:

i) InSAR processing

To overcome the decorrelation caused by changes in the permafrost landscape (e.g., freeze–thaw transitions and vegetation phenology), we generated interferograms with only short time intervals. The precision state vectors obtained from the ESA were applied to reduce the effects of inaccurate baselines. All the SLC images were coregistered to the stack reference of 20180807 acquisition for orbit 150 and 20180801 acquisition for orbit 48. After generating a coregistered stack of SLC images, interferograms were generated by each SAR image with its two sequential acquisitions. The temporal baselines of the individual interferograms ranged from 12 to 36 days, and the perpendicular baseline of all the interferometric pairs was < 200 m. Multilooking with 3 pixels in azimuth and 13 pixels in range was then performed to form a square pixel (~40 m) and reduce noise. To remove the topographic phase, the topographic phase was simulated using the SRTM DEM and subtracted from the interferogram. Next, we applied an adaptive spectral filter to produce differential interferograms. To unwrap the differential phase, the SNAPHU Minimum Cost Flow (MCF) phase unwrapping algorithm (Chen and Zebker, 2002) was applied. Two orbits covering an area of approximately 450 km×500 km were processed using ISCE software (https://github.com/isce-framework/isce2). To facilitate the processing of data over such a large area, coregistration and conversion between radar coordinates and geometric coordinate systems were accelerated by the aid of a graphics processing unit (GPU) under the Compute Unified Device Architecture (CUDA) framework.

ii) Deformation time series estimation

255    In this step, the network of unwrapped interferograms was inverted to construct a timeline of line-of-sight (LOS) displacement maps. A multilook 2 by 2 was applied to interferograms to reduce dataset size. Before the network inversion, we applied unwrapping error corrections by bridging reliable regions (Zhang et al., 2019b). The interferograms, generated by each SAR image with its two sequential acquisitions, all have averaged interferometric coherence above 0.7. Appendix Fig. A1 presents an overview of the interferogam

260    network and the averaged interferometric coherence. We applied a weighted least square (WLS) estimator to invert the network of interferograms into a time series. During the inversion, interferograms were weighted by the inverse of the phase variance of the whole interferogram (Zhang et al., 2019b). Different from some studies conducted in permafrost environments that presupposed deformation models to help solve the phase time series (Li et al., 2015; Chen et al., 2018), we did not preset any deformation and instead obtained the

265    raw phase time series by minimizing the phase residual. The time series of LOS displacements are relative to the first scene of the datasets and spatially relative to the reference point. The reference point was first set by selecting pixels with extremely high temporal coherence greater than 0.99.

After the raw phase time series were obtained, tropospheric delay correction, phase deramping, and

270    topographic residual correction were applied. The tropospheric delay was estimated in the satellite LOS direction using European Centre for Medium-Range Weather Forecasts (ECMWF) Fifth-generation Reanalysis (ERA-5) data. The processing was conducted in PyAPS software (Jolivet et al., 2014). The phase ramps, which might be caused by residual tropospheric and ionospheric delays, were estimated by a 2-D quadratic model based on reliable pixels and removed from the displacement time series at each acquisition.

275    The systematic topographic phase residuals caused by DEM errors were estimated based on the proportionality with the perpendicular baseline time series (Fattahi and Amelung, 2013). The processing described above was implemented by MintPy (Zhang et al., 2019b) (https://github.com/insarlab/MintPy).

Two indicators evaluated the quality of unwrapped phases and inverted raw phase time series: the phase

280    closure of interferogram triplets and temporal coherence. The phase unwrapping algorithms add integer number of $2\pi$ phase jumps to recover the unwrapped phase. Interferometric phase noise and discontinuities among different coherent regions may lead to wrong $2\pi$ jumps added to the phase field known as unwrapping error. Unwrapping errors can bias the estimated time series. For an interferogram triplet ($\Delta\phi^{ij}$, $\Delta\phi^{jk}$ and $\Delta\phi^{ik}$), unwrapping errors introduce a nonzero integer component $C_{int}^{ijk}$ in the closure phase $C^{ijk}$. Therefore, the

285    number of interferogram triplets with nonzero integer ambiguity $T_{int}$ can be used to detect unwrapping errors:

$$C^{ijk} = \Delta\varphi^{ij} + \Delta\varphi^{jk} - \Delta\varphi^{ik} \qquad (2)$$

$$C_{int}^{ijk} = \frac{C^{ijk} - \text{wrap}\,(C^{ijk})}{2\pi} \qquad (3)$$

$$T_{int} = \sum_{i=1}^{T} \left( C_{int}^{ijk}! = 0 \right) \qquad (4)$$

where $\Delta\varphi^{ij}$, $\Delta\varphi^{jk}$ and $\Delta\varphi^{ik}$ are the three unwrapped interferometric phases generated from the SAR acquisitions at $t_i$, $t_j$ and $t_k$, respectively; wrap is an operator that wraps each input number into $[-\pi, \pi)$; and T is the number of interferogram triplets. A triplet without unwrapping errors has $C_{int}^{ijk} \equiv 0$.

The second index, temporal coherence, represents the consistency of the time series with the network of interferograms (Pepe and Lanari, 2006):

$$\gamma_{\text{temp}} = \frac{1}{M} \left| H^T \exp\left[ j(\Delta\phi - A\hat{\phi}) \right] \right| \tag{5}$$

where (for N SAR images and M interferograms) $\Delta\phi$ is the unwrapped interferometric phase; A is the $M \times (N-1)$ design matrix indicating the acquisition pairs used for interferograms generation (consisting of -1, 0 and 1 for each row with -1 for the reference acquisition, 1 for the secondary acquisition and 0 for all other acquisitions (Berardino et al., 2002)); $\hat{\phi}$ denotes the estimated time series; H is an M×1 all-ones column vector; and j is the imaginary unit.

Temporal coherence varies from 0 to 1: pixels with values closer to 1 are considered reliable, whereas pixels with values closer to zero are considered unreliable. A threshold of 0.7 is recommended to be used for a dense network of interferograms. In this study, we used a threshold of 0.85; the pixels with temporal coherence below this threshold were masked from the final result.

iii) Reference point refinement and geocoding

In the natural environment, exposed bedrock in flat terrain is normally selected as the reference point; however, because such exposed bedrock is scarce in the study area, we took great care in the selection of reference points. We selected a reference point near the boundary of Selin Co watershed not affected by permafrost in dry and flat terrain. The residual phases from atmospheric distortions and tectonic movements on the TP are difficult to remove completely in such a large-scale extent. However, the effect could be reduced by setting the reference near the study area. The reference area was homogeneous and had interferometric coherence close to 1. Thus, we adjusted the displacements relative to this reference area, the location of the reference area is marked in Fig. 1. Finally, we geocoded the deformation time series to the WGS84 coordinate system with a grid spacing of 0.0009°×0.0009° and then reprojected it onto the Albers equal area conic system with a 100 m×100 m grid size. To minimize the effects of extreme values, we also applied a 3-size moving window filtering to the deformation time series.

**3.3.2 Extraction of periodic (seasonal) amplitudes and inter-annual deformation rates**

The surface deformation in permafrost terrain exhibits the characteristics of both long-term linear deformation and seasonal oscillations (uplift in winter and spring and subsidence in summer and autumn) (Daout et al., 2017; Li et al., 2015). Therefore, we applied a sinusoidal (seasonal) function plus a linear (interannual) trend to the displacement time series of each image pixel using Eq. (6).

$$d(t) = a \cdot t + A \cdot \sin\left(\frac{2\pi}{T} \cdot t + \varphi\right) + c \tag{6}$$

where $t$ is the time interval with respect to the first SAR image acquisition date, a is the long-term deformation rate, A is the periodic (seasonal) amplitude, $T$ is the period of the seasonal undulation (assumed to be one year), $\varphi$ is the initial phase, and c is the residual term. a, $A$, $\varphi$ and c are the coefficients to be determined. The peak-to-peak periodic (seasonal) deformation is twice the periodic amplitude of $A$. The seasonal amplitude shown in this work refers to the amount of $A$, not peak-to-peak deformation amount of 2A.

For each orbit, we extracted the LOS periodic (seasonal) amplitude and long-term deformation rate pixel by pixel from the deformation time series and then mosaiced the results from the two orbits together. The spatial grids of the incidence angles from the two orbits were mosaiced as well.

### 3.3.3 Deformation from the LOS direction to the vertical direction

For flat terrain, deformation is caused mainly by freeze–thaw cycles within the permafrost layer and occurs predominantly in the vertical direction. Hence, assuming no horizontal displacement, the observed deformation in the line of the sight (LOS) direction was converted into the vertical direction using Eq. (7) by dividing the deformation value by the cosine of the incidence angle (the incidence angle ranges of orbit 48 and orbit 150 of the S1 satellites are listed in Table 1):

$$d_v = d_{LOS}/\cos(\theta) \tag{7}$$

where $d_{LOS}$ is the observed deformation along the LOS direction, $d_v$ is the deformation in the vertical direction, and $\theta$ is the incidence angle of the sensor.

### 3.4 Conversion from surface deformation into ground ice meltwater contributions

A considerable amount of ground ice is always buried in permafrost regions, especially just below the permafrost table (Cheng, 1983; Mackay, 1983; French and Harbor, 2013). Thawing of the uppermost permafrost layer is always accompanied by the compaction of sediment and subsidence of the ground surface due to the melting of super-saturated ground ice (French, 2017). Hence, the higher the ice content in permafrost, the larger the surface subsidence occur as it was thawed. In this study, we assume that the cumulated long-term settlement is equal to the thickness of ground ice melted, and then release to the hydrological cycle. We converted the deformation rate into the ground ice meltwater via the following steps:

i) Masking areas with slope angles >10°

On steep slopes, deformation occurs mainly as downslope movements driven by gravity (Buckel et al., 2021; Reinosch et al., 2020); thus, we considered only areas with slope angles below 10°. This threshold of 10° was adopted based on previous works (Reinosch et al., 2020; Buckel et al., 2021).

ii) Masking areas with the LOS periodic (seasonal) amplitudes ≤1.5 mm or long-term velocities ≤2.5 mm/a

These thresholds were similarly set based on previous works (Daout et al., 2017; Buckel et al., 2021) and field surveys. The periodic seasonal threshold was used to mask areas that were unaffected by permafrost activity (because they do not experience periodic frost heave and thaw subsidence) but exhibited continuous

surface uplift or subsidence. Areas with periodic (seasonal) amplitudes below 1.5 mm and long-term (inter-annual) velocities less than 2.5 mm/a were likely unmoving considering distortions in the InSAR phase and DEM error.

iii) Conversion from surface deformation into ground ice meltwater

Selin Co is located in the lowest area of the watershed, and the water released from thawing permafrost eventually enters the lake. The long-term deformation represents the elevation changes produced by ground ice change. Using Eq. (8), by multiplying the grid cell size, we can obtain the ice volume change for each grid cell and then sum among all the cells to estimate the total ice volume contribution. Because the density of water is ~1.0 g/cm$^3$ and that of ice is ~0.91 g/cm$^3$, the ice volume amount is then multiplied by a factor of 0.91 to convert to the corresponding water volume:

$$\Delta V_{water} = 0.91 \cdot \Delta V_{ice} = 0.91 \cdot \sum \Delta h \cdot C_{grid} = 0.91 \cdot \sum d \cdot C_{grid} \tag{8}$$

where $\Delta V_{ice}$ is the change in the ground ice volume, $\Delta h$ is the elevation change produced by the ice change, $C_{grid}$ is the area of a grid cell, and $d_v$ is the long-term deformation rate in the vertical direction.

## 4. Results

### 4.1 Lake water storage changes

We analyzed the changes in the lake water storage of three large lakes within the Selin Co watershed: Selin Co, Ngoin Co, and the combination of Wuru Co & Qiagui Co. Table 5 lists the surface extents of the investigated lakes on the Landsat acquisition dates. Selin Co expanded at a rate of 10.3 km$^2$/a from 2015 to 2020. Fig. 4 illustrates the water surface elevation time series of the investigated lakes derived by ICESat-2 during October 2018 and 2020. During this period, the surface water increased at a rate of 0.2 m/a for Selin Co. Table 6 summarizes the averaged water surface elevation from each lake, considering all the elevation measurements within each year. The tracks of the elevation measurements in these years are plotted in Fig. 2(a-c). To calculate the changes in the lake water storage of Selin Co, Eq. (1) was applied taking the areas of 2408.1 km$^2$ in 2018 and 2441.2 km$^2$ in 2020 and taking the water surface elevation change of ~0.4 m between these two years; then, the change in lake volume from 2018 to 2020 was estimated, and finally, the annual volume change rate was obtained by dividing the results of these two years. The annual rate of change in the lake volume of Selin Co during 2018–2020 was ~485×10$^6$ m$^3$/a.

**Table 5 Lake areas from 2015 to 2020.**

| Lake | Area (km$^2$) | | | | | | | |
|------|------|------|------|------|------|------|------|------|
| | 2015 | 2016 | 2017 | 2018 | 2019 | 2020 | Change rate (km$^2$/a) | |
| **Selin Co** | 2398.7 | 2377.1 | 2393.8 | 2408.1 | 2421.1 | 2441.2 | 10.3 | |
| **Co Ngoin** | 276.6 | 276.7 | 281.8 | 281.6 | 285.2 | 284.1 | 1.8 | |
| **Wuru Co & Qiagui Co** | 432.5 | 437.2 | 432.5 | 452.5 | 447.2 | 443.0 | 2.9 | |
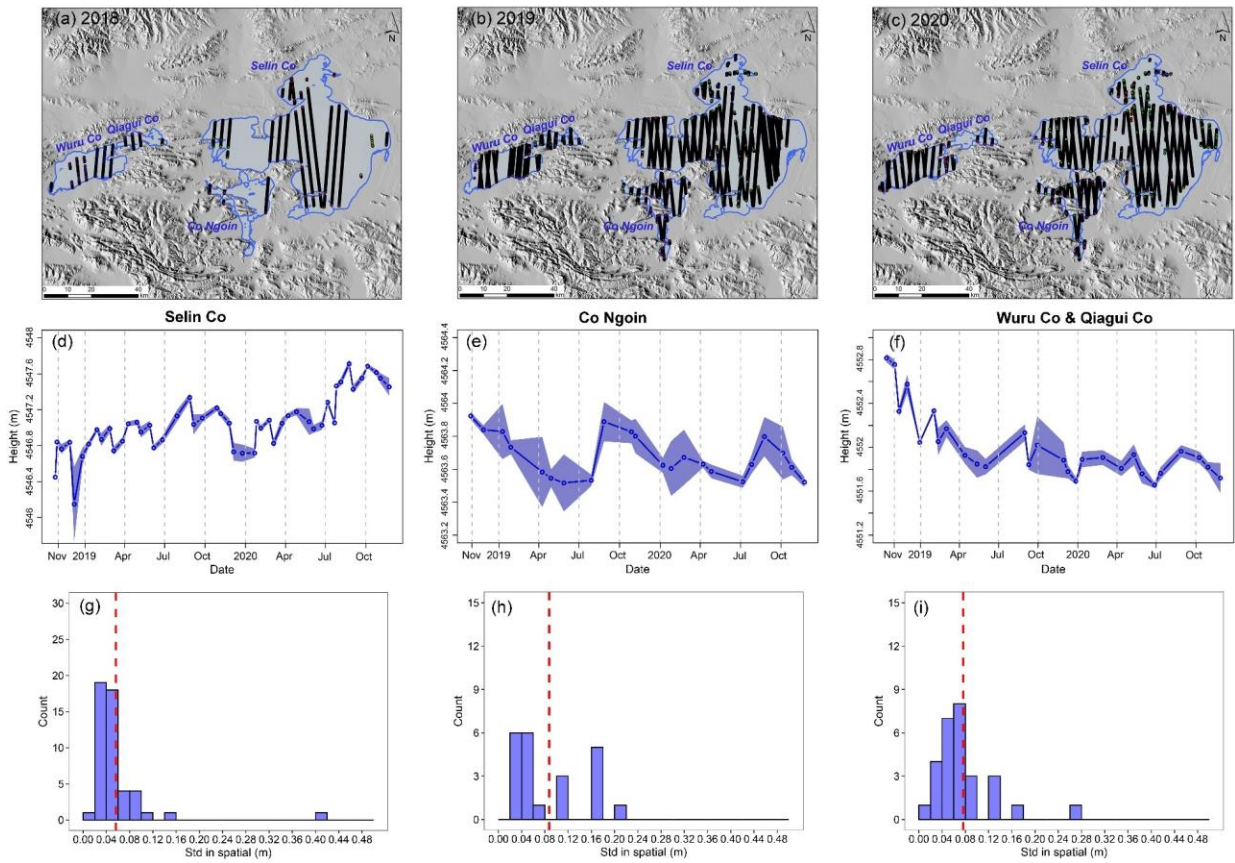
**Figure 4 Water surface elevations of the three lakes. Subfigures (a)-(c) show tracks of the elevation measurements for each year. Subfigures (d)-(f) show the ICESat-2 derived elevations. The solid lines indicate the average values of all elevation measurements within the lake on a given date. The light-colored areas show the mean ± one standard deviation. Subfigures (g)-(i) further show histograms of the standard deviations of the water surface elevation of the lake from all acquisition dates. Red dashed line indicates the mean value.**

**Table 6 Lake elevations from 2018 to 2020, presented as the mean ± one standard deviation of all elevation measurements of the lake within the year. The tracks of the ICESat-2 elevation measurements are shown in Fig. 4 (a)-(c).**

| Lake | Surface water elevation (m) | | |
|---|---|---|---|
| | 2018 | 2019 | 2020 |
| **Selin Co** | 4546.72 ± 0.10 | 4546.97 ± 0.17 | 4547.20 ± 0.26 |
| **Ngoin Co** | 4563.86 ± 0.05 | 4563.74 ± 0.20 | 4563.63 ± 0.14 |
| **Wuru Co & Qiagui Co** | 4552.51 ± 0.26 | 4551.97 ± 0.20 | 4551.87 ± 0.09 |

**4.2 Ground surface deformation**

**4.2.1 Deformation at the borehole and GPR survey sites**

400 The deformation time series at the seven borehole sites are shown in Fig. 5. The detected deformation properties are highly consistent with the field surveys. Sites SLC03 and SLC04 displayed the largest seasonal amplitudes of 13.8 mm and 16.6 mm, respectively; among all the borehole sites, these sites are the wettest and have the most developed vegetation cover, i.e., alpine swamp meadows with coverage higher than 90%. These seasonal amplitudes are to a large extent caused by the water–ice phase changes in the freeze–thaw

405 cycle and are thus extremely sensitive to the water content in the active layer (Chen et al., 2020). Permafrost can hold more water in the active layer than seasonally frozen ground; this is why site SLC05 in seasonally frozen ground displayed the smallest seasonal oscillation of 0.5 mm. Excess ice was found in the SLC04 borehole; correspondingly, the largest subsidence velocity of 18.9 mm/a was observed at this site. Likewise, SLC02 and SLC03, in which ground ice was found, showed different levels of subsidence. Site SLC05, which

410 is seasonally frozen and located in a river valley between two rivers, exhibited an uplift of 3.2 mm/a, which might be because of sedimentation.

We also examined the deformation characteristics at the GPR survey sites. Among the twenty GPR segments where permafrost existence was confirmed, the seasonal amplitudes were all larger than 2.0 mm, with a

415 maximum amplitude of 16.2 mm and an average of 8.2 mm.
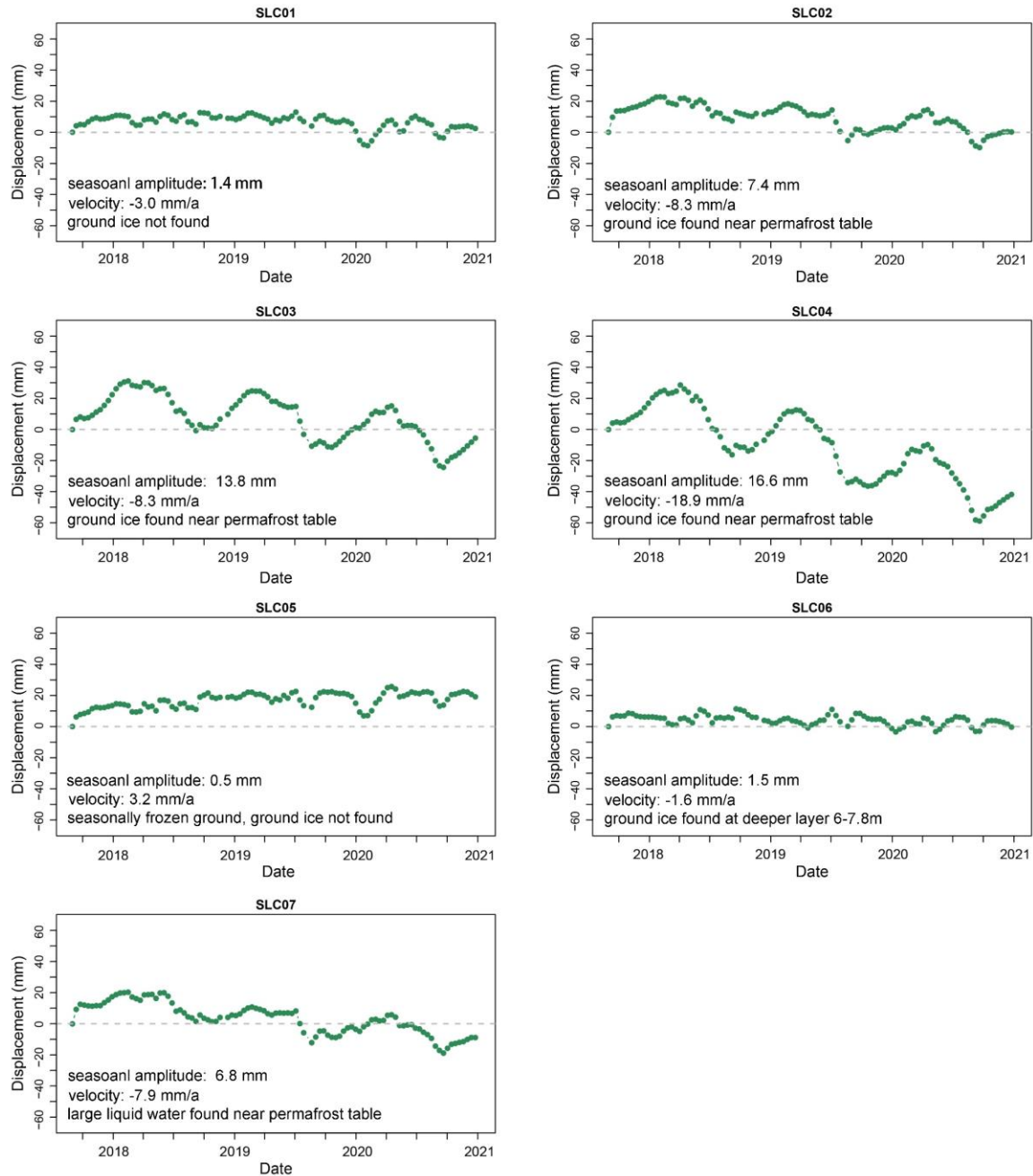
**Figure 5 LOS deformation time series at the seven borehole sites. Positive values represent uplift and negative values represent subsidence relative to the first scene of the S1 datasets.**

420

### 4.2.2 Spatial distributions of the seasonal amplitude and long-term deformation rate

Fig. 6 and Fig. 7 show the spatial distributions of the periodic (seasonal) amplitude and long-term (inter-annual) deformation rate, both of which are in accordance with the permafrost distribution map (Fig. 1). The boundary in Fig. 1 differentiating continuous permafrost from seasonally frozen ground exactly matches the

425    boundaries observed for the seasonal amplitudes in Fig. 6 and the long-term deformation rates in Fig. 7. As

shown in Fig. 6–7, widespread and large subsidence and large seasonal amplitudes are located in the upstream portion of the Zhajiazangbu subbasin southeast of Mt. Geladandong, where widespread continuous permafrost is present. Appendix Fig. A3 provides the deformation map covering the field investigation region.
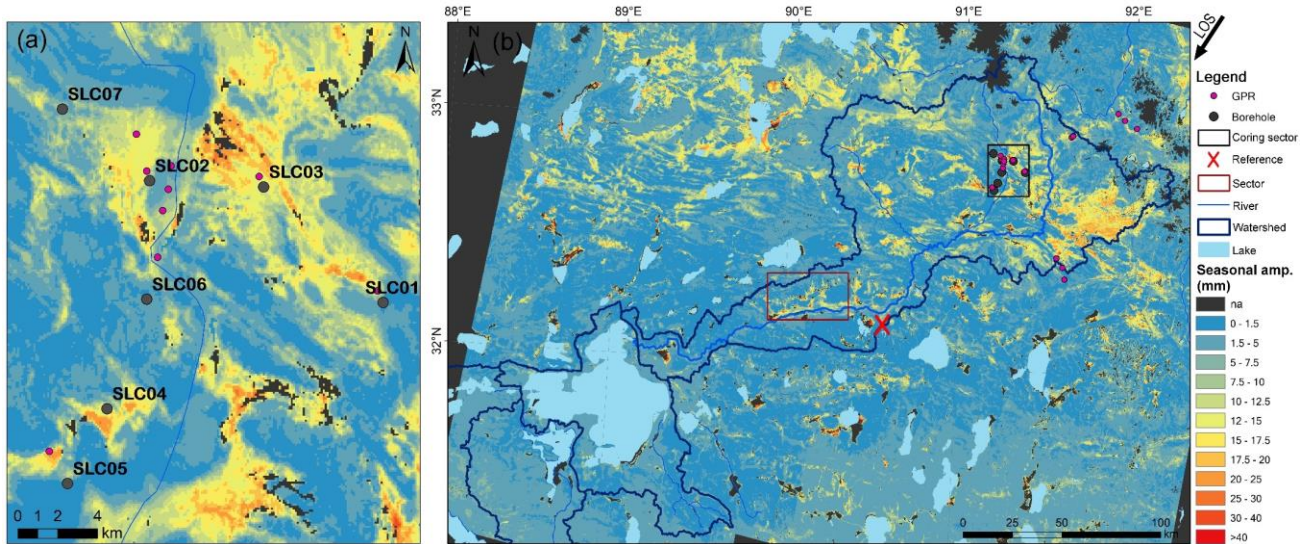
430    **Figure 6 Map of the periodic (seasonal) amplitude in the satellite LOS direction. Subfigure (b) shows an enlarged view of the coring area (black sector in subfigure (a)). Dark grey colored "na" means the information could not be retrieved because of no data or decorrelation.**
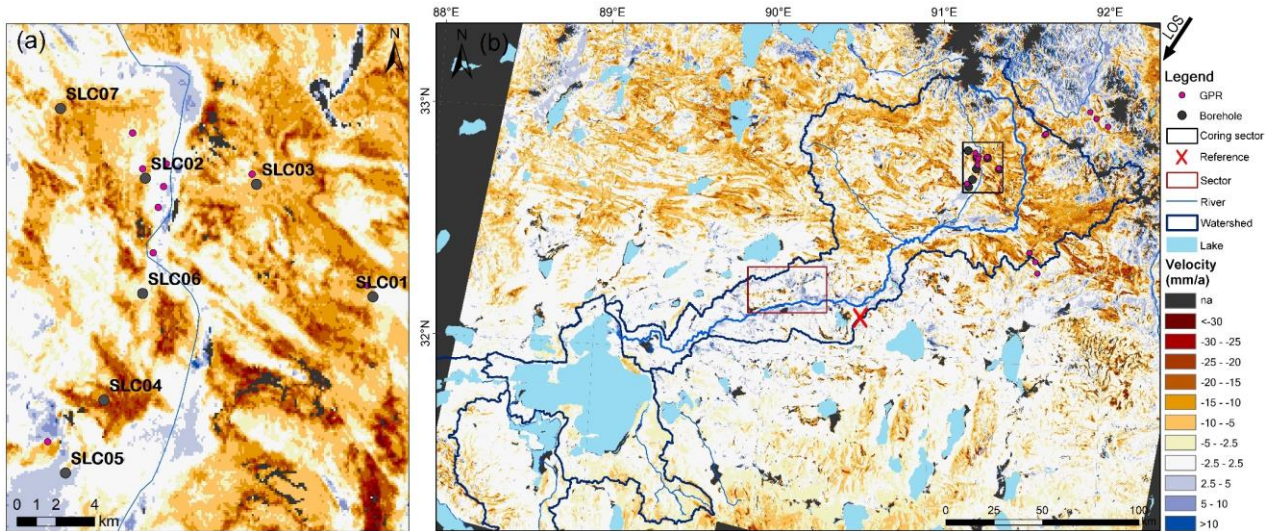
**Figure 7 Map of the inter-annual deformation velocity in the satellite LOS direction. Subfigure (b) shows an**
435    **enlarged view of the coring area (black sector in subfigure (a)). Dark grey colored "na" means the information could not be retrieved because of no data or decorrelation.**

Fig. 8 shows a density plot of the seasonal amplitude versus the deformation rate. Subsidence in the Selin Co watershed was normally between 5 and 20 mm/a (see the statistical details in Table 8) but reached 50 mm/a

440    in certain regions, reflecting highly excessive volumes of ice and rapid ice loss in this region. The seasonal amplitude ranged between 0 mm and 60 mm within the watershed area. In the Zhajiazangbu subbasin with extensive permafrost, among the areas with deformation rates greater than 2.5 mm/a, 0.1% of them had

seasonal amplitudes greater than 30 mm, 2.2% had amplitudes between 20 mm and 30 mm, 24.1% had amplitudes between 10 mm and 20 mm, 23% had amplitudes between 5 mm and 10 mm, and 50.6% had amplitudes of less than 5 mm; overall, the average seasonal amplitude was 6.9 mm.
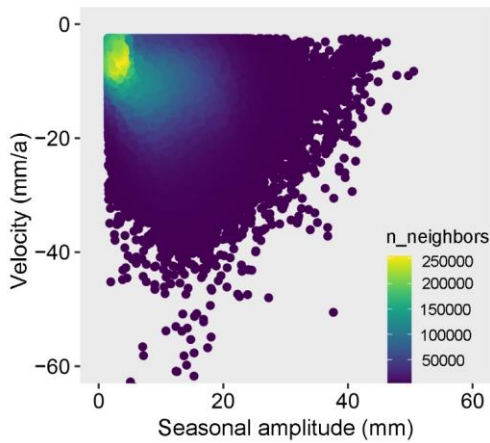
**Figure 8 Distribution of the LOS seasonal amplitude versus the LOS deformation velocity within the Selin Co watershed, in all 6.57 ×10^5 valid pixels.**

**Table 8 Characteristics of terrain subsidence in the Selin Co basin.**

| Basin | Average (mm) | Percentage of subsidence (%) | | | | |
|---|---|---|---|---|---|---|
| | | -5 ~ -2.5 mm | -10 ~ -5 mm | -20 ~ -10 mm | -30 ~ -20 mm | < -30 mm |
| **Zhajiazangbu subbasin** | -10.6 | 13.8 | 36.7 | 44.3 | 4.9 | 0.3 |
| **Boquzangbu subbasin** | -5.3 | 61.8 | 30.3 | 7.5 | 0.4 | 0 |
| **Overall** | -10.3 | 16.3 | 36.3 | 42.3 | 4.7 | 0.3 |

### 4.3 Water contributed by ground ice melting

Fig. 9 shows a map of the potential volume of water contributed by changes in permafrost ground ice. Table 9 lists the statistics of the potential water contribution volume for the Selin Co basin. The main contribution comes from the Zhajiazangbu subbasin, where the permafrost coverage is 66.2%, whereas the contribution from the Boquzangbu subbasin is limited. The potential rate of ground ice meltwater generation was $55.6\times10^6$ $m^3$/a in the Zhajiazangbu subbasin and $1.9\times10^6$ $m^3$/a in the Boquzangbu subbasin, and the overall rate was $57.4\times10^6$ $m^3$/a. Compared to the rate of change in the lake water storage of Selin Co ($485\times10^6$ $m^3$/a), we obtained a ground ice meltwater contribution ratio of 11.8%. Converting the potential water contribution volume into the runoff depth within the watershed yields a 2.7 mm/a increase in the runoff depth.
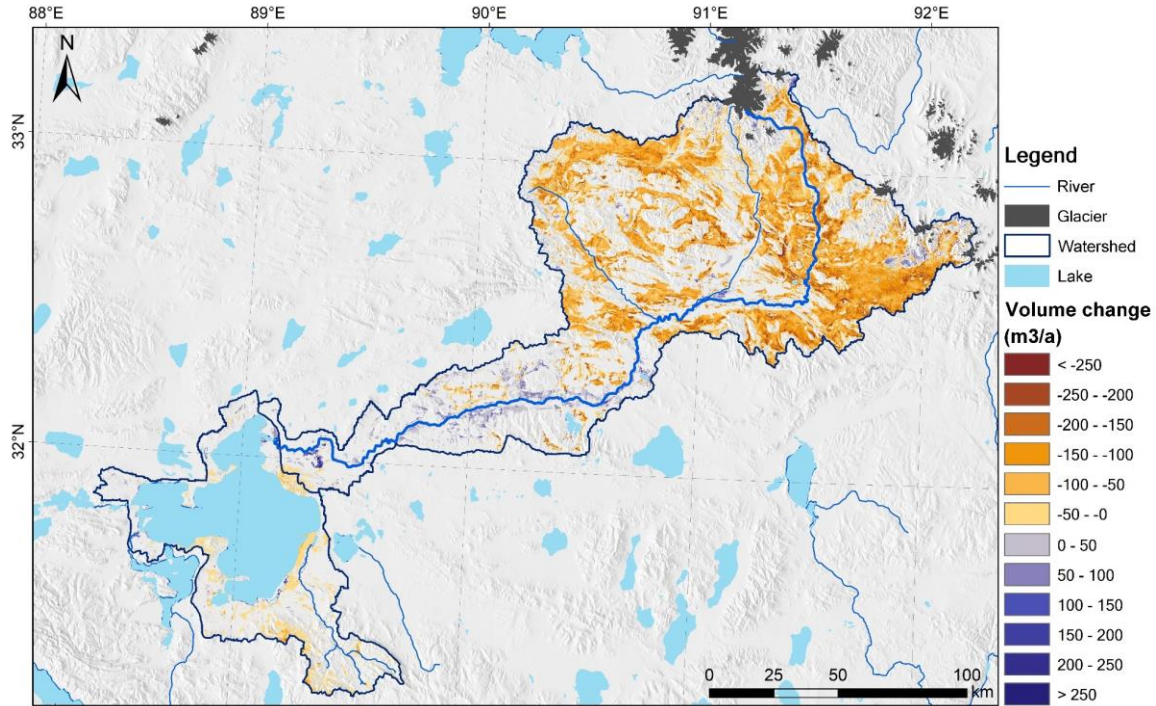
**Figure 9 Map of the potential ground ice melting water supply. The grid color represents the grid cell's yearly ground ice melting water supply volume, with negative values indicating ground ice loss and meltwater release.**

465

**Table 9 Yearly volume of ground ice meltwater contribution in the Selin Co watershed.**

| Basin | Water volume ($10^6$ m$^3$/a) | Runoff depth (mm) |
|---|---|---|
| Zhajiazangbu subbasin | 55.6 | 3.5 |
| Boquzangbu subbasin | 1.9 | 0.3 |
| Overall | 57.4 | 2.7 |
| Ratio of lake volume increasement | 11.8% | |

### 4.4 Uncertainty analysis

### 4.4.1 Uncertainties and accuracies of lake volume changes

470  Fig. 4(d) clearly shows that the water surface elevation of Selin Co has increased gradually, although seasonal fluctuations are evident as well. Selin Co has 49 ICESat-2 acquisitions during the investigation period (Fig. 4(g)), and 69.4% of these acquisitions correspond to elevation measurements with a standard deviation smaller than 0.05 m within the lake. This means that the average values of all elevation measurements within the lake could represent the lake's elevation on a given date. To evaluate the accuracy of the resulting lake

475  area extent, we validated the classification results by randomly selecting 1000 pixels from the Landsat images and visually examining the classification results. The classification accuracy reached approximately 0.98.

Our analysis shows that during the period of 2018–2020, the water level increased at a rate of ~0.2 m/a, the lake area increased at a rate of 10.3 km²/a, and the lake water storage increased at a rate of 485×10⁶ m³/a. These values are compared with those recorded in previous studies in Fig. 10. Lake area change information are from (Zhu et al., 2019b; Qiao et al., 2019; Meng et al., 2012; Sun et al., 2020; Zhang et al., 2020; Deij et al., 2018); water level change information are from (Meng et al., 2012; Lei et al., 2013; Doin et al., 2015; Zhang et al., 2013; Sun et al., 2020; Hwang et al., 2019; Zhang et al., 2020; Zhu et al., 2019a); and water volume information are from (Zhu et al., 2019b; Qiao et al., 2019; Treichler et al., 2019; Sun et al., 2020; Zhang et al., 2013; Li et al., 2019). As illustrated in Fig. 10, the expansion of Selin Co was slow before 2000, with lake area and volume increases of 9.1 km²/a and 368×10⁶ m³/a, respectively. Then, in the period of 2000–2005, the lake expanded extremely fast, with the water level increasing at an approximate rate of 1.0 m/a and the lake area and volume increasing at rates of 60.7 km²/a and 1576×10⁶ m³/a, respectively. After 2005, however, these rates of increase slowed down, with those of the lake area and lake water storage slowing to only 12.6 km²/a and 553×10⁶ m³/a during 2005–2017, respectively, and the rate of increase in the water surface elevation slowing to 0.2 m/a during 2007–2011 (Doin et al., 2015). Overall, the values retrieved in this study are all within the ranges of the historical values and are closest to the values after the 2010s.
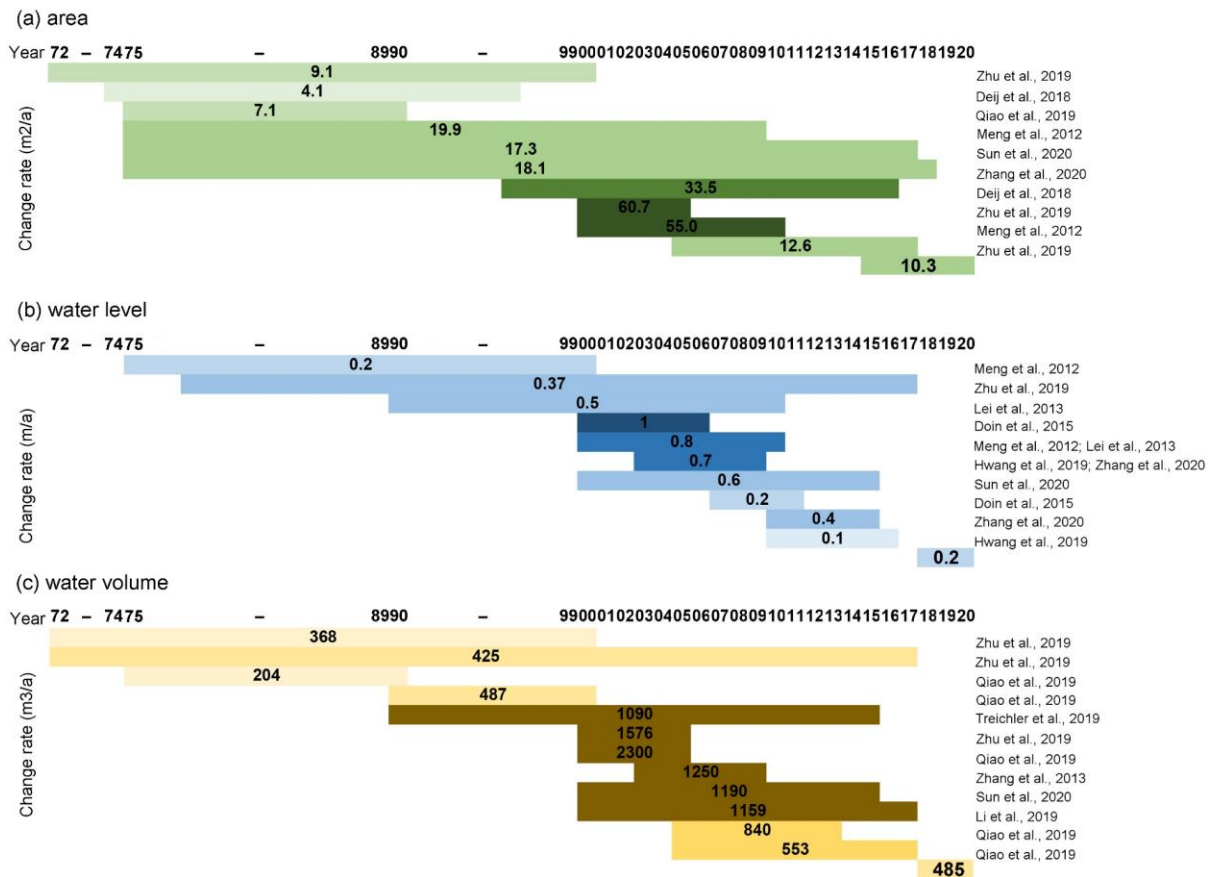
**Figure 10 Comparisons of the changes in the lake area (subfigure a) water surface elevation (b) and lake volume (c) of Selin Co with historical values.**

### 4.4.2 Uncertainties and accuracies of deformation

Two indicators evaluated the quality of unwrapped phases and inverted raw phase time series: the phase closure of interferogram triplets and temporal coherence. Fig. 11 shows the spatial distribution of the number of interferogram triplets with nonzero integer ambiguity $T_{int}$ (Eq (4)), with the histogram illustrating the distribution of $T_{int}$ values within the Selin Co watershed excluding glaciers and water bodies. The areas having $T_{int}$ smaller than three take part 95% of the watershed, while 72.3% of the watershed has $T_{int}$ value of zero (no wrapping error on all the interferograms). The $T_{int}$ evaluated the quality of original interferometric unwrapped phases, the unwrapping errors could be further reduced by bridging reliable regions before network revision (Zhang et al., 2019b).
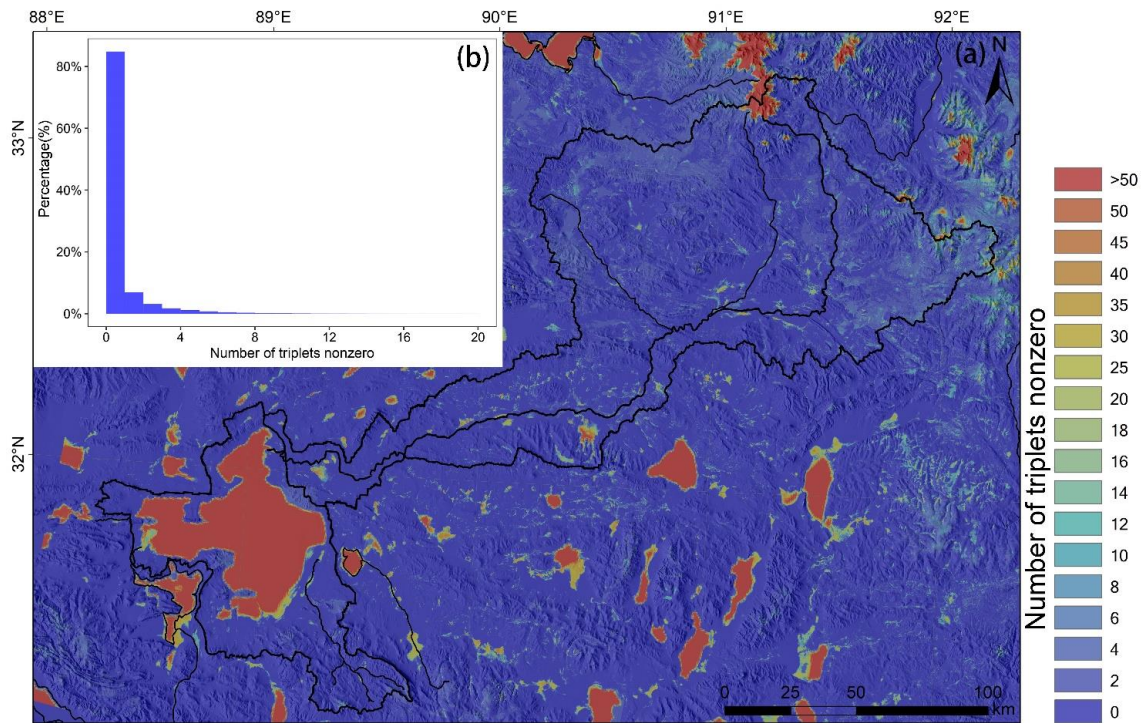
**Figure 11 (a) Map of the number of interferogram triplets with nonzero integer ambiguity $T_{int}$ (Eq(4)), (b) histogram illustrating the distribution of $T_{int}$ values within the Selin Co watershed excluding glaciers and water bodies.**

Fig. 12 shows the spatial distribution of temporal coherence (Eq. (5)), which is used to evaluate the quality of raw phase time series. 99.0% of the watershed has temporal coherence higher than 0.8, 98.1% has temporal coherence higher than 0.85, 96.0% has temporal coherence higher than 0.9 and 89.1% has temporal coherence higher than 0.95.
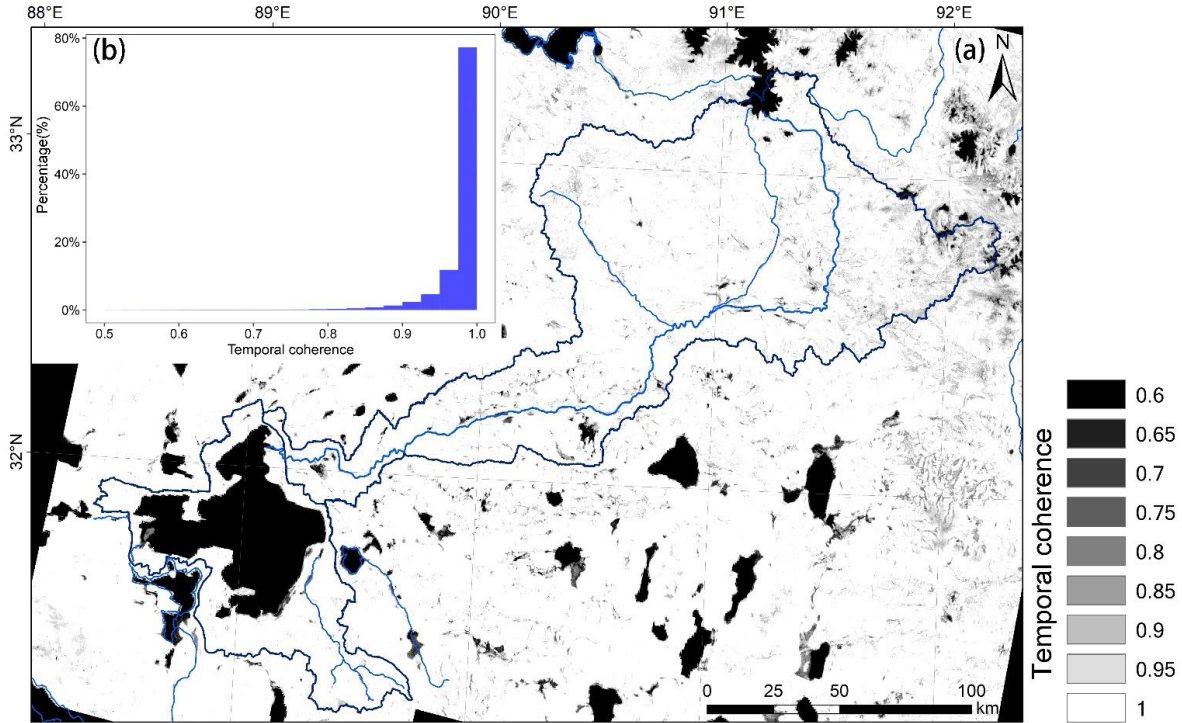
**Figure 12 (a) Map of temporal coherence (Eq(5)), (b) histogram illustrating the distribution of temporal coherence values within the Selin Co watershed excluding glaciers and water bodies.**

The Selin Co basin was covered by two orbits of S1 images: orbit 48 and orbit 150. Appendix Fig. A2 presents the amplitude and long-term velocity retrieved from orbit 48 and orbit 150, respectively. In the large overlapping area covering 270 km × 55 km, the results from orbit 150 and orbit 48 reveal identical deformation characters. This confirms that the seasonal amplitudes and deformation rates extracted from the two orbits are robust even though the acquisitions from the two orbits are not the same (Table 3).

In addition, the deformation characteristics were compared with the observations from the boreholes, and excellent agreement was achieved. We also validated the SBAS-InSAR-derived deformation (which has the same processing flow as applied in this study) with the in situ leveling measurements at the Wudaoliang site on the TP; the relative error was found to be 14.8% regarding the long-term deformation rate (Zhou et al., 2019). Furthermore, we are currently operating an automatic deformation monitoring device in the watershed, and it is expected to provide an independent validation reference.

### 4.4.3 Uncertainties in the slope angle threshold in the estimation of ground ice meltwater

During the estimation process, we masked regions with slopes steeper than the threshold of 10°. We also tested the impact of setting slope thresholds of 15° and 20° on the results. When using the 15° or 20° threshold,

535 the volume of meltwater released changed by less than 1%. Hence, the setting of the threshold does not greatly influence the final prediction.

## 5. Discussion

### 5.1 Uplift displacement signal

In addition to widespread subsidence detected in the upstream of Zhajiazangbu of the continuous permafrost
540 environment, the uplift signal was also observed in the sporadic permafrost environment in the middle stream of the Zhajiazangbu subbasin, also near some drained ponds. Fig. 13 shows a sector (location marked in red rectangle in Fig. 1, 6–7), in which both subsidence and uplift signals are detected. The mean annual air temperature is -2.0°C, calculated based on ERA5-Land air temperature hourly reanalysis data during 2017–2020. For a better interpretation, Landsat optical image and elevation with were also presented. The spatial
545 distribution pattern of deformation aligns with landscape and topography very well. Large seasonal amplitude only appears in the vegetated and wet area, which indicates the water storage in the active layer in a certain way. Uplift signals are generally at the slope feet. Fig. 13(e)–(h) displays the deformation time series of four sites s1-s4 from high elevation to low elevation. Site s2 is stable, viewing from seasonal amplitude and long-term deformation velocity. The subsidence of site s3 is the result of ground ice melting, confirmed by the
550 large periodic seasonal amplitude caused by frost heave and thaw subsidence in the active layer. The uplift signals of site s1 and site 4 are worth exploring, especially site s4. Site s4 has a possibility of being related to ground ice aggradation since it also exhibits moderate seasonal amplitude, but it is more likely related to sediment accumulation or groundwater table rise regarding its location.
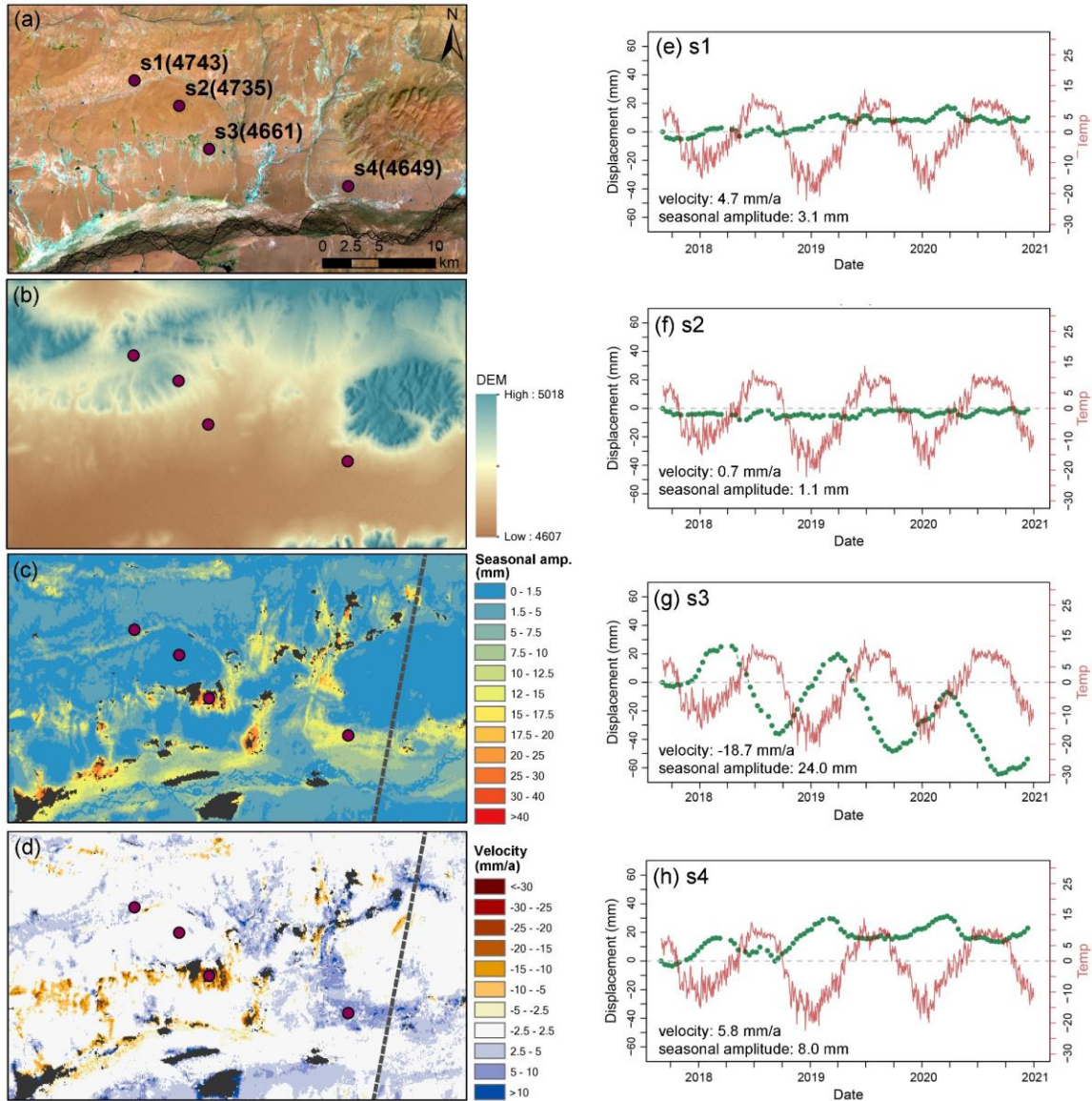
**Figure 13 Deformation characters. This sector is marked with the red rectangle in Fig. 1 and 7-8. (a) Landsat 8 image (red: SWIR1, green: NIR, blue: red). (b) DEM overlapped on the hillshade, which is calculated using DEM with the Sentinel-1 incidence angle and azimuth angle. (c)(d) are seasonal deformation amplitude and long-term deformation velocity, respectively. The grey dashed line delineates the track boundary of orbit 150. (e)-(h) are deformation time series of marked sites. The elevetation (m a.s.l.) of the sites are labeled in brackets in subfigure (a). Air temperature in red color is from ERA5-Land air temperature reanalysis data. Deformations are in the LOS direction.**

Previous research normally focuses on the thaw subsidence signal on the TP, and less attention has been given to the uplift signal. Some of the uplift signals might be related to deposition or the rise of the groundwater table. Some of the uplift signals might be caused by ground ice aggradation. A sufficient water supply accompanied by strong evaporation (cooling effect, energy is taken away) might facilitate the upward freezing of previously unfrozen (or seasonally frozen) sediment. Ground ice aggradation is slightly surprising in the overall warming climate of the study area. However, the upward freezing of previously unfrozen (or

seasonally frozen) sediment is still possible and may occur because of sediment accretion (e.g., deltaic and

570 alluvial sedimentation) (French, 2017). A previous study (Daout et al., 2020) also detected a complex deformation signal in the permafrost on the northeastern TP and hypothesized that the uplift deformation in lowland regions was caused by excess meltwater pooling, which triggered an increase in the segregation of ice near the permafrost table. On the TP, new permafrost forming is detected on the exposed bottom of Zonag Lake (Zhang et al., 2022). Thus, on the TP, it might be common for degradation and aggradation of ground

575 ice to both occur in permafrost environments, with degradation representing the dominant pattern and aggradation existing in local areas. Currently, most studies focus on permafrost subsidence signals, and few studies have studied permafrost ground ice aggradation and the causes of uplift signals in local environments. Nevertheless, the uplift signals in the permafrost environment on the TP are worthy of additional research, and further details on the Selin Co basin are expected to be unveiled and supplemented by the next field

580 survey.

**5.2 Water contribution by permafrost ground ice melting in the Selin Co watershed**

In this study, we assumed that the amount of surface settlement corresponds to the release of the same volume of ground ice as a result of compressing the thawing ice-rich permafrost layer and that the released water

585 eventually enters Selin Co; the potential water contribution volume was estimated accordingly. However, the effect of permafrost degradation on the terrestrial water cycle is complicated (Ma et al., 2020). A gradually thickening active layer may retain more water in the soil layer; thus, endorheic basins may collect more water during the thawing season. Additionally, the increase in the active layer thickness due to the warming climate could lead to enhanced evaporation. Furthermore, in permafrost terrain, the interactions between groundwater

590 and surface water are restricted. With continued permafrost degradation, the rates of groundwater recharge and discharge are expected to increase since the impermeable barrier provided by permafrost weakens. Ultimately, the melting of ground ice can lead to the infiltration of more surface water into groundwater aquifers in the basin, thereby increasing groundwater storage in the basin (Bense et al., 2012; Zhang et al., 2017).

595

Based on the detected deformation, we estimated that the volumetric rate of water being released due to the melting of ground ice could reach $57.4 \times 10^6$ $m^3$/a for the Zhajiazangbu and Boquzangbu subbasins. If the Alizangbu and Zhagenzangbu subbasins are included, the volume contributed by ground ice melting could be even larger. According to the permafrost distribution statistics (Table 1), the Zhajiazangbu and

600 Boquzangbu subbasins together have a permafrost area of 10791 $km^2$, while the other two subbasins, the Alizangbu and Zhagenzangbu, have a combined permafrost area of only 2613 $km^2$, approximately 25% of the permafrost area in the two northern subbasins. A map of the ground ice distribution on the TP (Zhao and Sheng, 2019) likewise illustrates that the ground ice volumes in the Alizangbu and Zhagenzangbu subbasins are small compared to that in the Zhajiazangbu subbasin. Moreover, the water released from ground ice

605     melting does not directly supply Selin Co in the Alizangbu and Zhagenzangbu subbasins; rather, this meltwater supplies Ngoin Co and Wuru Co & Qiagui Co first. In addition, during 2018–2020, the surface water level slightly dropped in Ngoin Co and Wuru Co & Qiagui Co (Fig. 4 and Table 5). Thus, the water supply from other lakes to Selin Co might be limited considering the circumstances stated above and thus was not incorporated into the calculation in the current study. In addition, there are some wet areas facing

610     strong decorrelation (1.9% of watershed area has temporal decorrelation smaller than 0.85 and masked), where deformation information could not be retrieved. However, these areas usually experience very large subsidence. If taking into account of these areas, the ground ice meltwater contribution could be higher. If only the retrieved subsidence signal is considered, the ground ice meltwater volume contribution is $57.4 \times 10^6$ $m^3/a$, accounting for 11.8% of the lake volume increase. This result is consistent with a previous model

615     simulation of the water supply of permafrost degradation to the lake volume increase of the endorheic basins on the TP (Zhang et al., 2017), which estimated the water supply by multiplying the active layer thickening rate and the average ground ice content and revealed that permafrost degradation contributed ~12% of the water supply to the lake volume increase.

620     Our three-year study period is relatively short compared to the continuous period of the growth of Selin Co from the 1970s to the present. The deformation rate and the lake water storage increasing rate in the other periods might be different from those in 2017–2020. C-band ERS, ENVISAT, and L-band ALOS PALSAR provide historical SAR data from the 1990s to the 2010s and will be processed and analyzed in a future study.

## 6. Conclusions

625     This is the first study to quantify the contribution of ground ice melting to the expansion of Selin Co. We monitored the surface deformation using the SBAS-InSAR technique over a large area of approximately 450 km×500 km across the Selin Co basin and then utilized the long-term deformation rates to estimate the potential volume of water being released via ground ice melting. Then, this amount was compared with the lake volume change during the same period, and the contribution ratio was derived. SBAS-InSAR monitoring

630     during 2017–2020 exposed widespread and large subsidence in the upstream section of the Zhajiazangbu subbasin, which is underlain by widespread, continuous permafrost. Subsidence normally occurred between 5 and 20 mm/a (78.6%), indicating highly excess ice and rapid ice loss in the region. During the same period, the lake water storage increased at a rate of approximately $485 \times 10^6$ $m^3/a$, and the potential rate at which water was being released due to ground ice melting reached $57.4 \times 10^6$ $m^3/a$, contributing 11.8% of the lake

635     volume increase. The uplift signals in some lowland areas with a sufficient water supply and in drained ponds are worth noting, and more details will be revealed through future field surveys. This study is especially helpful for explaining the rapid expansion of Selin Co and equilibrating the water balance at the watershed scale. More importantly, the proposed method can be easily extended to other watersheds underlain by permafrost to help us better understand the hydrological changes in these watersheds.

**Acknowledgments**

This work was supported by research grants from the National Natural Science Foundation of China (No. 42001054 and 41931180), the Second Tibetan Plateau Scientific Expedition and Research (STEP) program (No. 2019QZKK0201), and the Natural Science Foundation of the Jiangsu Province (BK20200828). We are also grateful to the logistics staff who provided tremendous help during the field campaign.

**Data availability**

Sentinel-1 Level 1 single-look complex (SLC) images can be accessed from the Alaska Satellite Facility (https://search.asf.alaska.edu/) or Copernicus Open Access Hub (https://scihub.copernicus.eu/). The lake area extents during 2015–2017 were from the datasets "The lakes larger than 1km$^2$ in Tibetan Plateau (V2.0)", provided by the National Tibetan Plateau Data Center.

**Author contribution**

L. Wang and L. Zhao designed the study and wrote the manuscript. L. Zhao directed the project. L. Wang, H. Zhou, S. Liu, and C. Li performed the surface deformation analysis; X. Li performed the lake water level analysis; E. Du conducted GPR survey and interpretation; L. Zhao, G. Liu, D. Zou, H. Zhou, Z. Sun, E. Du, Y. Xiao, G. Hu, S. Liu, Z. Li, C. Wang, Y Qiao and T. Wu conducted the field works and borehole drillings. L. Wang, L. Zhao, H. Zhou, S. Liu, D. Zou, G. Liu, E. Du interpretated and discussed the results.

**Competing interests**

No conflict of interest.

**References**

Bense, V., Kooi, H., Ferguson, G., and Read, T.: Permafrost degradation as a control on hydrogeological regime shifts in a warming climate, Journal of Geophysical Research: Earth Surface, 117, 2012.

Berardino, P., Fornaro, G., Lanari, R., and Sansosti, E.: A new algorithm for surface deformation monitoring based on small baseline differential SAR interferograms, Geoscience and Remote Sensing, IEEE Transactions on, 40, 2375-2383, 2002.

Bian, D., Bian, B., La, B., Wang, C., and Chen, T.: The Response of Water Level of Selin Co to Climate Change during 1975-2008 (in Chinese), Acta Geographica Sinica, 65, 2010.

Brun, F., Treichler, D., Shean, D., and Immerzeel, W. W.: Limited contribution of glacier mass loss to the recent increase in Tibetan Plateau lake volume, Frontiers in Earth Science, 8, 495, 2020.

Buckel, J., Reinosch, E., Hördt, A., Zhang, F., Riedel, B., Gerke, M., Schwalb, A., and Mäusbacher, R.: Insights into a remote cryosphere: a multi-method approach to assess permafrost occurrence at the Qugaqie basin, western Nyainqêntanglha Range, Tibetan Plateau, The Cryosphere, 15, 149-168, 2021.

Chen, C. W. and Zebker, H. A.: Phase unwrapping for large SAR interferograms: Statistical segmentation and generalized network models, IEEE Transactions on Geoscience and Remote Sensing, 40, 1709-1719, 2002.

Chen, J., Liu, L., Zhang, T., Cao, B., and Lin, H.: Using persistent scatterer interferometry to map and quantify permafrost thaw subsidence: A case study of Eboling Mountain on the Qinghai-Tibet Plateau, Journal of Geophysical Research: Earth Surface, 123, 2663-2676, 2018.

Chen, J., Wu, Y., O'Connor, M., Cardenas, M. B., Schaefer, K., Michaelides, R., and Kling, G.: Active layer freeze-thaw and water storage dynamics in permafrost environments inferred from InSAR, Remote Sensing of Environment, 248, 112007, 2020.

Chen, J., Wu, T., Zou, D., Liu, L., Wu, X., Gong, W., Zhu, X., Li, R., Hao, J., and Hu, G.: Magnitudes and patterns of large-scale permafrost ground deformation revealed by Sentinel-1 InSAR on the central Qinghai-Tibet Plateau, Remote Sensing of Environment, 268, 112778, 2022.

680    Cheng, G.: The mechanism of repeated-segregation for the formation of thick layered ground ice, Cold Regions Science and Technology, 8, 57-66, 1983.

Daout, S., Dini, B., Haeberli, W., Doin, M.-P., and Parsons, B.: Ice loss in the Northeastern Tibetan Plateau permafrost as seen by 16 yr of ESA SAR missions, Earth and Planetary Science Letters, 545, 116404, 2020.

Daout, S., Doin, M. P., Peltzer, G., Socquet, A., and Lasserre, C.: Large-scale InSAR monitoring of permafrost freeze-thaw cycles

685    on the Tibetan Plateau, Geophysical Research Letters, 44, 901-909, 2017.

Deij, Y., Nima, J., Qianba, O., Zeng, L., and Luosang, Q.: Lake Area Variation of Selin Tso in 1975 ~ 2016 and Its Influential Factors, Plateau and Mountain Meteorology Research, 38, 2018.

Doin, M. P., Twardzik, C., Ducret, G., Lasserre, C., Guillaso, S., and Jianbao, S.: InSAR measurement of the deformation around Siling Co Lake: Inferences on the lower crust viscosity in central Tibet, Journal of Geophysical Research: Solid Earth, 120, 5290-

690    5310, 2015.

Farinotti, D., Huss, M., Fürst, J. J., Landmann, J., Machguth, H., Maussion, F., and Pandit, A.: A consensus estimate for the ice thickness distribution of all glaciers on Earth, Nature Geoscience, 12, 168-173, 2019.

Fattahi, H. and Amelung, F.: DEM error correction in InSAR time series, IEEE Transactions on Geoscience and Remote Sensing, 51, 4249-4259, 2013.

695    French, H. and Harbor, J.: 8.1 The Development and History of Glacial and Periglacial Geomorphology, Treatise on Geomorphology, Academic Press, https://doi.org/10.1016/B978-0-12-374739-6.00190-1, 2013.

French, H. M.: The periglacial environment, John Wiley & Sons2017.

Günther, F., Overduin, P. P., Yakshina, I. A., Opel, T., Baranskaya, A. V., and Grigoriev, M. N.: Observing Muostakh disappear: permafrost thaw subsidence and erosion of a ground-ice-rich island in response to arctic summer warming and sea ice reduction,

700    The Cryosphere, 9, 151-178, 2015.

Guo, W., Liu, S., Xu, J., Wu, L., Shangguan, D., Yao, X., Wei, J., Bao, W., Yu, P., and Liu, Q.: The second Chinese glacier inventory: data, methods and results, Journal of Glaciology, 61, 357-372, 2015.

Guo, Y., Zhang, Y., Ma, N., Xu, J., and Zhang, T.: Long-term changes in evaporation over Siling Co Lake on the Tibetan Plateau and its impact on recent rapid lake expansion, Atmospheric research, 216, 141-150, 2019.

705    Hwang, C.-w., Cheng, Y. S., Yang, W. H., Zhang, G., Huang, Y. R., Shen, W. B., and Pan, Y.: Lake level changes in the Tibetan Plateau from Cryosat-2, SARAL, ICESat, and Jason-2 altimeters, Terr. Atmos. Ocean. Sci, 30, 1-18, 2019.

Jin, H., Huang, Y., Bense, V. F., Ma, Q., Marchenko, S. S., Shepelev, V. V., Hu, Y., Liang, S., Spektor, V. V., and Jin, X.: Permafrost Degradation and Its Hydrogeological Impacts, Water, 14, 372, 2022.

Jolivet, R., Agram, P. S., Lin, N. Y., Simons, M., Doin, M. P., Peltzer, G., and Li, Z.: Improving InSAR geodesy using global atmospheric

710    models, Journal of Geophysical Research: Solid Earth, 119, 2324-2341, 2014.

Kokelj, S. V. and Jorgenson, M.: Advances in thermokarst research, Permafrost and Periglacial Processes, 24, 108-119, 2013.

Lanari, R., Lundgren, P., Manzo, M., and Casu, F.: Satellite radar interferometry time series analysis of surface deformation for Los Angeles, California, Geophysical Research Letters, 31, 2004.

Lantuit, H. and Pollard, W.: Fifty years of coastal erosion and retrogressive thaw slump activity on Herschel Island, southern

715    Beaufort Sea, Yukon Territory, Canada, Geomorphology, 95, 84-102, 2008.

Lei, Y., Yao, T., Bird, B. W., Yang, K., Zhai, J., and Sheng, Y.: Coherent lake growth on the central Tibetan Plateau since the 1970s: Characterization and attribution, Journal of Hydrology, 483, 61-67, 2013.

Lei, Y., Yang, K., Wang, B., Sheng, Y., Bird, B. W., Zhang, G., and Tian, L.: Response of inland lake dynamics over the Tibetan Plateau to climate change, Climatic Change, 125, 281-290, 2014.

720    Li, X., Long, D., Huang, Q., Han, P., Zhao, F., and Wada, Y.: High-temporal-resolution water level and storage change data sets for lakes on the Tibetan Plateau during 2000–2017 using multiple altimetric missions and Landsat-derived lake shoreline positions, Earth System Science Data, 11, 1603-1627, 2019.

Li, Y., Liao, J., Guo, H., Liu, Z., and Shen, G.: Patterns and potential drivers of dramatic changes in Tibetan lakes, 1972–2010, PloS one, 9, e111890, 2014.

725    Li, Z., Zhao, R., Hu, J., Wen, L., Feng, G., Zhang, Z., and Wang, Q.: InSAR analysis of surface deformation over permafrost to estimate active layer thickness based on one-dimensional heat transfer model of soils, Scientific reports, 5, 2015.

Liu, L., Schaefer, K., Zhang, T., and Wahr, J.: Estimating 1992–2000 average active layer thickness on the Alaskan North Slope from remotely sensed surface subsidence, Journal of Geophysical Research: Earth Surface, 117, 2012a.

Liu, S., Guo, W., and Xu, J.: The second glacier inventory dataset of China (version 1.0) (2006-2011) [dataset],

730    10.3972/glacier.001.2013.db, 2012b.

Lu, P., Han, J., Li, Z., Xu, R., Li, R., Hao, T., and Qiao, G.: Lake outburst accelerated permafrost degradation on Qinghai-Tibet Plateau, Remote Sensing of Environment, 249, 112011, 2020.

Ma, Q., Jin, H.-J., Bense, V. F., Dong-Liang, L., Marchenko, S. S., Harris, S. A., and Lan, Y.-C.: Impacts of degrading permafrost on streamflow in the source area of Yellow River on the Qinghai-Tibet Plateau, China, Advances in Climate Change Research, 2020.

735    Mackay, J. R.: Downward water movement into frozen ground, western arctic coast, Canada, Canadian Journal of Earth Sciences, 20, 120-134, 1983.

Meng, K., Shi, X., Wang, E., and Liu, F.: High-altitude salt lake elevation changes and glacial ablation in Central Tibet, 2000–2010, Chinese Science Bulletin, 57, 525-534, 2012.

Pepe, A. and Lanari, R.: On the extension of the minimum cost flow algorithm for phase unwrapping of multitemporal differential

740    SAR interferograms, IEEE Transactions on Geoscience and remote sensing, 44, 2374-2383, 2006.

Qiao, B., Zhu, L., and Yang, R.: Temporal-spatial differences in lake water storage changes and their links to climate change throughout the Tibetan Plateau, Remote Sensing of Environment, 222, 232-243, 2019.

Reinosch, E., Buckel, J., Dong, J., Gerke, M., Baade, J., and Riedel, B.: InSAR time series analysis of seasonal surface displacement dynamics on the Tibetan Plateau, The Cryosphere, 14, 1633-1650, 2020.

745     Shiklomanov, N. I., Streletskiy, D. A., Little, J. D., and Nelson, F. E.: Isotropic thaw subsidence in undisturbed permafrost landscapes, Geophysical Research Letters, 40, 6356-6361, 2013.

Song, C., Huang, B., Richards, K., Ke, L., and Hien Phan, V.: Accelerated lake expansion on the Tibetan Plateau in the 2000s: Induced by glacial melting or other processes?, Water Resources Research, 50, 3170-3186, 2014.

Streletskiy, D. A., Shiklomanov, N. I., Little, J. D., Nelson, F. E., Brown, J., Nyland, K. E., and Klene, A. E.: Thaw subsidence in
750     undisturbed tundra landscapes, Barrow, Alaska, 1962–2015, Permafrost and Periglacial Processes, 28, 566-572, 2016.

Sun, F., Ma, R., He, B., Zhao, X., Zeng, Y., Zhang, S., and Tang, S.: Changing Patterns of Lakes on The Southern Tibetan Plateau Based on Multi-Source Satellite Data, Remote Sensing, 12, 3450, 2020.

Tong, K., Su, F., and Xu, B.: Quantifying the contribution of glacier meltwater in the expansion of the largest lake in Tibet, Journal of Geophysical Research: Atmospheres, 121, 11,158-111,173, 2016.

755     Treichler, D., Kääb, A., Salzmann, N., and Xu, C.-Y.: Recent glacier and lake changes in High Mountain Asia and their relation to precipitation changes, The Cryosphere, 13, 2977-3005, 2019.

Usai, S.: A least squares database approach for SAR interferometric data, Geoscience and Remote Sensing, IEEE Transactions on, 41, 753-760, 2003.

Wu, Z., Zhao, L., Liu, L., Zhu, R., Gao, Z., Qiao, Y., Tian, L., Zhou, H., and Xie, M.: Surface-deformation monitoring in the permafrost
760     regions over the Tibetan Plateau, using Sentinel-1 data, Sciences in Cold and Arid Regions, 10, 114-125, 2018.

Yang, Y., Wu, Q., Yun, H., Jin, H., and Zhang, Z.: Evaluation of the hydrological contributions of permafrost to the thermokarst lakes on the Qinghai–Tibet Plateau using stable isotopes, Global and planetary change, 140, 1-8, 2016.

Yang, Y., Wu, Q., Jin, H., Wang, Q., Huang, Y., Luo, D., Gao, S., and Jin, X.: Delineating the hydrological processes and hydraulic connectivities under permafrost degradation on Northeastern Qinghai-Tibet Plateau, China, Journal of hydrology, 569, 359-372,
765     2019.

Zhang, G.: The lakes larger than 1km2 in Tibetan Plateau (V2.0) (1970s-2018) [dataset], 10.11888/Hydro.tpdc.270303, 2019.

Zhang, G., Chen, W., and Xie, H.: Tibetan Plateau's lake level and volume changes from NASA's ICESat/ICESat-2 and Landsat Missions, Geophysical Research Letters, 46, 13107-13118, 2019a.

Zhang, G., Yao, T., and Kang, S.: Water balance estimates of ten greatest lakes in China using ICESat and Landsat data (in Chinese),
770     Chin Sci Bull, 58, 2664-2678, 2013.

Zhang, G., Bolch, T., Chen, W., and Crétaux, J.-F.: Comprehensive estimation of lake volume changes on the Tibetan Plateau during 1976–2019 and basin-wide glacier contribution, Science of the Total Environment, 772, 145463, 2021a.

Zhang, G., Ran, Y., Wan, W., Luo, W., Chen, W., Xu, F., and Li, X.: 100 years of lake evolution over the Qinghai–Tibet Plateau, Earth System Science Data, 13, 3951-3966, 2021b.

775     Zhang, G., Yao, T., Shum, C., Yi, S., Yang, K., Xie, H., Feng, W., Bolch, T., Wang, L., and Behrangi, A.: Lake volume and groundwater storage variations in Tibetan Plateau's endorheic basin, Geophysical Research Letters, 44, 5550-5560, 2017.

Zhang, G., Yao, T., Xie, H., Yang, K., Zhu, L., Shum, C., Bolch, T., Yi, S., Allen, S., and Jiang, L.: Response of Tibetan Plateau's lakes to climate changes: trend, pattern, and mechanisms, Earth-Science Reviews, 103269, 2020.

Zhang, Y., Fattahi, H., and Amelung, F.: Small baseline InSAR time series analysis: Unwrapping error correction and noise
780     reduction, Computers & Geosciences, 133, 104331, 2019b.

Zhang, Y., Xie, C., Wu, T., Zhao, L., Wu, J., Wu, X., Li, R., Hu, G., Liu, G., and Wang, W.: New permafrost is forming on the exposed bottom of Zonag Lake on the Qinghai-Tibet Plateau, Science of The Total Environment, 152879, 2022.

Zhao, L. and Sheng, Y.: Permafrost and environment changes on the QinghaiTibetan Plateau (in Chinese), Science Press, Beijing, China2019.

785     Zhao, L., Hu, G., Zou, D., Wu, X., Ma, L., Sun, Z., Yuan, L., Zhou, H., and Liu, S.: Permafrost Changes and Its Effects on Hydrological Processes on Qinghai-Tibet Plateau (in Chinese), Bulletin of the Chinese Academy of Sciences, 34, 1233-1246, 2019.

Zhao, L., Zou, D., Du, E., Hu, G., Pang, Q., Xiao, Y., Li, R., Sheng, Y., Wu, X., Sun, Z., Wang, L., Wang, C., Ma, L., Zhou, H., and Liu, S.: Changing climate and the permafrost environment on the Qinghai-Tibet (Xizang) Plateau, Permafrost and Periglacial Processes, 10.1002/ppp.2056, 2020.

790     Zhou, H., Zhao, L., Tian, l., Wu, Z., Xie, M., Yuan, L., Ni, J., Qiao, Y., Gao, Z., and Shi, J.: Monitoring and analysis of surface deformation in the permafrost area of Wudaoliang on the Tibetan Plateau based on Sentinel-1 data (in Chinese), Journal of Glaciology and Geocryology, 41, 525-536, 2019.

Zhu, L., Zhang, G., Yang, R., Liu, C., Yang, K., Qiao, B., and Han, B.: Lake Variations on Tibetan Plateau of Recent 40 Years and Future Changing Tendency (in Chinese), Bulletin of the Chinese Academy of Sciences, 34, 1254-1263, 2019a.

795     Zhu, L., Wang, J., Ju, J., Ma, N., Zhang, Y., Liu, C., Han, B., Liu, L., Wang, M., and Ma, Q.: Climatic and lake environmental changes in the Serling Co region of Tibet over a variety of timescales, Science Bulletin, 64, 422-424, 2019b.

Zou, D., Zhao, L., Yu, S., Chen, J., Hu, G., Wu, T., Wu, J., Xie, C., Wu, X., and Pang, Q.: A new map of permafrost distribution on the Tibetan Plateau, The Cryosphere, 11, 2527, 2017.

Zwieback, S. and Meyer, F. J.: Top-of-permafrost ground ice indicated by remotely sensed late-season subsidence, The
800     Cryosphere, 15, 2041-2055, 2021.

**Appendix**
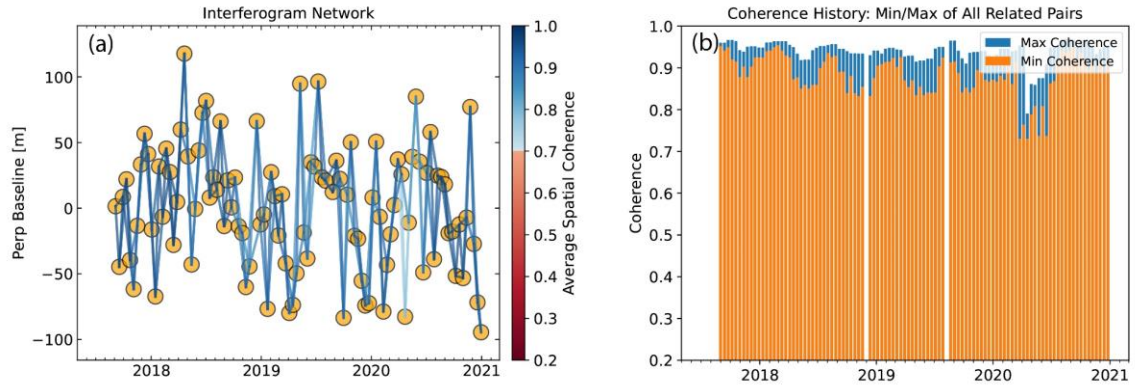
**Fig. A1 (a) Network of interferograms for deformation time series estimation, color-coded by average coherence of the interferograms. Circles represent the acquisition dates, and lines represent the interferograms. (b) Average coherence of all related pairs for each SAR acquisition date.**
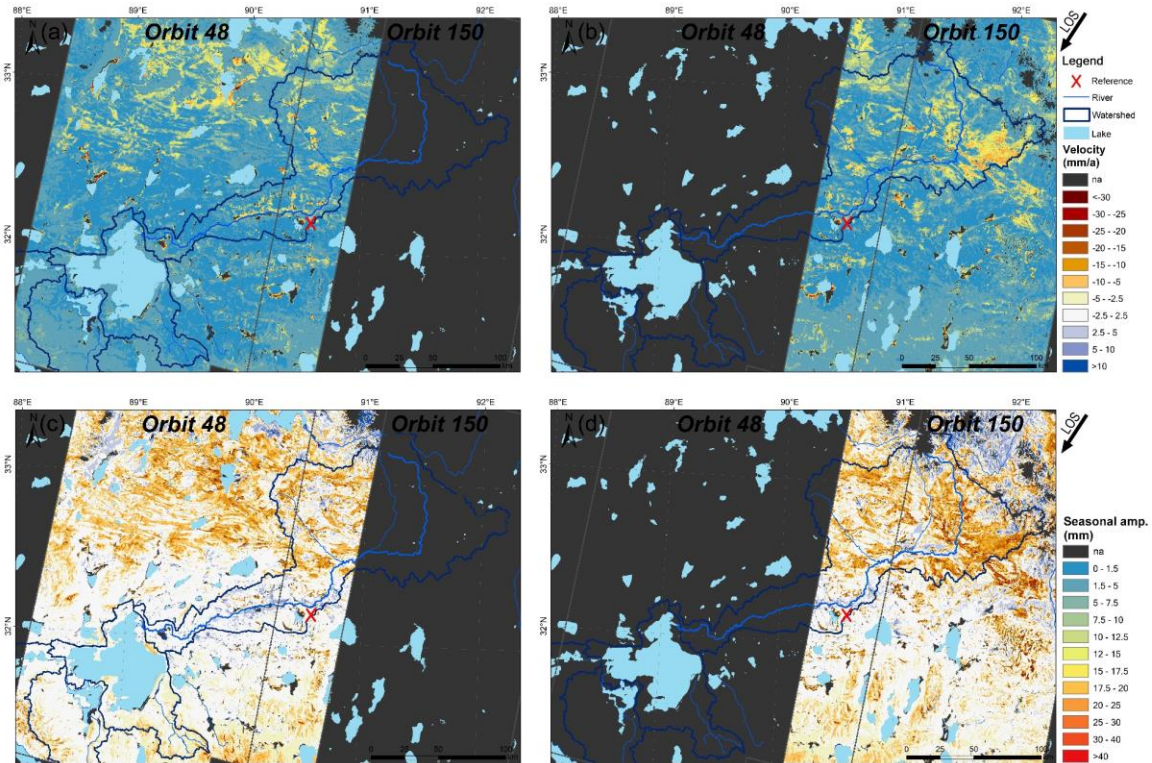
**Fig. A2 Map of the periodic (seasonal) amplitude (a)(b) and long-term velocity (c)(d) retrieved from orbit 48 (a)(c) and orbit 150 (b)(d), respectively, all are in the satellite LOS direction.**

810
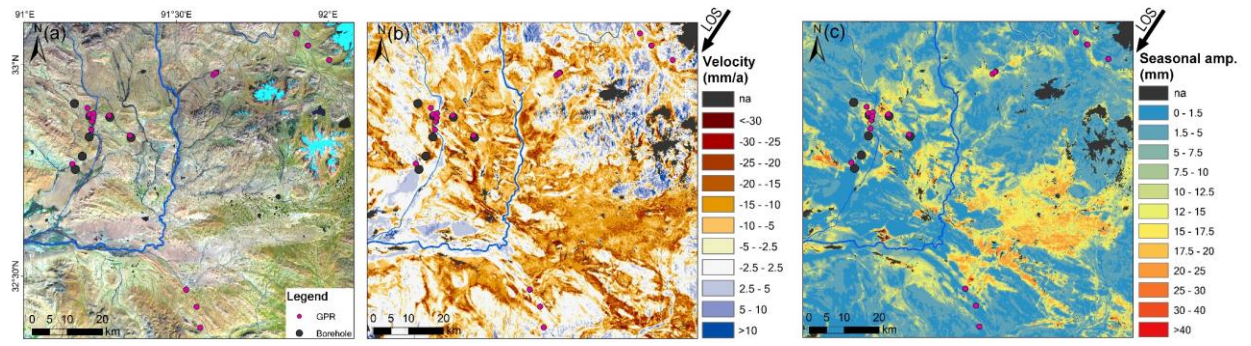
**Fig. A3 Maps of the GPR and borehole regions, (a) Landsat 8 image acquired in October 2020 (red: SWIR1, green: NIR, blue: red), with GPR and borehole sites marked, (b) long-term deformation velocity, (c) seasonal deformation amplitude.**

815